Supplementary Information to "Unveiling clean two-dimensional discrete time crystals on a digital quantum computer"

Kazuya Shinjo[1], Kazuhiro Seki[2], Tomonori Shirakawa[2,3,4,5], Rong-Yang Sun[2,3,4], and Seiji Yunoki[1,2,3,5]

[1]Computational Quantum Matter Research Team, RIKEN Center for Emergent Matter Science (CEMS), Wako, Saitama 351-0198, Japan
[2]Quantum Computational Science Research Team, RIKEN Center for Quantum Computing (RQC), Wako, Saitama 351-0198, Japan
[3]Computational Materials Science Research Team, RIKEN Center for Computational Science (R-CCS), Kobe, Hyogo 650-0047, Japan
[4]RIKEN Interdisciplinary Theoretical and Mathematical Sciences Program (iTHEMS), Wako, Saitama 351-0198, Japan
[5]Computational Condensed Matter Physics Laboratory, RIKEN Pioneering Research Institute (PRI), Saitama 351-0198, Japan

CONTENTS

I. SUPPLEMENTARY NOTE 1: QUANTUM DEVICE CONDITIONS

The experimental data presented in this study were obtained using the IBM Quantum Heron processor, ibm_torino, via cloud access, predominantly during the period from January 1 to January 31, 2024. Throughout this duration, the average relaxation and dephasing times T_1 and T_2, as well as the average readout assignment error rate, across all qubits were 165μs, 138μs, and 0.03, respectively. Additionally, the average error rate of CZ gates and the average duration of CZ gates across all qubits were 0.006 and 101ns, respectively. Notably, no significant deviations were observed in the data obtained on different dates, indicating the consistency and stability of the quantum device utilised for this study.

II. SUPPLEMENTARY NOTE 2: RESULTS FOR A HEAVY-HEXAGONAL LATTICE OF $L = 28$ QUBITS

Supplementary Figure 1 shows the error-unmitigated raw data of the averaged magnetisation $\langle \hat{Z}_{\rm avg}(t)\rangle_0$ for up to 100 time steps obtained for the $L = 28$ system using ibm_torino (see Fig. 4a). Here, the average is performed over the same set A of qubits as described in the main text, i.e., $A = \{63, 64, 65, 66, 67, 68, 69, 70, 71\}$. To mitigate errors in the raw data for $\theta_x \neq \pi$, the results for the trivial cases with $\theta_x = \pi$ are utilised, as detailed in Eq. (4).

Comparing with the results obtained by the state-vector method [1] in Supplementary Figures 2 and 3, we find that error-mitigated values $\langle \hat{Z}_{\rm avg}(t)\rangle$ are generally in good agreement with the numerically exact values, although deviations become apparent in some cases, particularly for long time steps.

To assess the accuracy of various tensor network methods, including matrix product state (MPS) [2] and two-dimensional tensor network state (2dTNS) methods (for details of our 2dTNS simulations, see Sec. IX), we compare the results of $\langle \hat{Z}_{\rm avg}(t)\rangle$ obtained by these methods with the numerically exact results calculated by the state-vector method in Supplementary Figures 4 and 5. As shown in Supplementary Figures 4a-4c and 5a-5c, when $\theta_x = 0.9\pi$, $\langle \hat{Z}_{\rm avg}(t)\rangle$ obtained by these tensor network methods with relatively small bond dimensions χ (MPS with $\chi = 300$ and 2dTNS with $\chi = 40$) sufficiently converge consistently to the numerically exact values, even for time steps up to 100. However, as shown in Supplementary Figures 4d-4f and 5d-5f, when

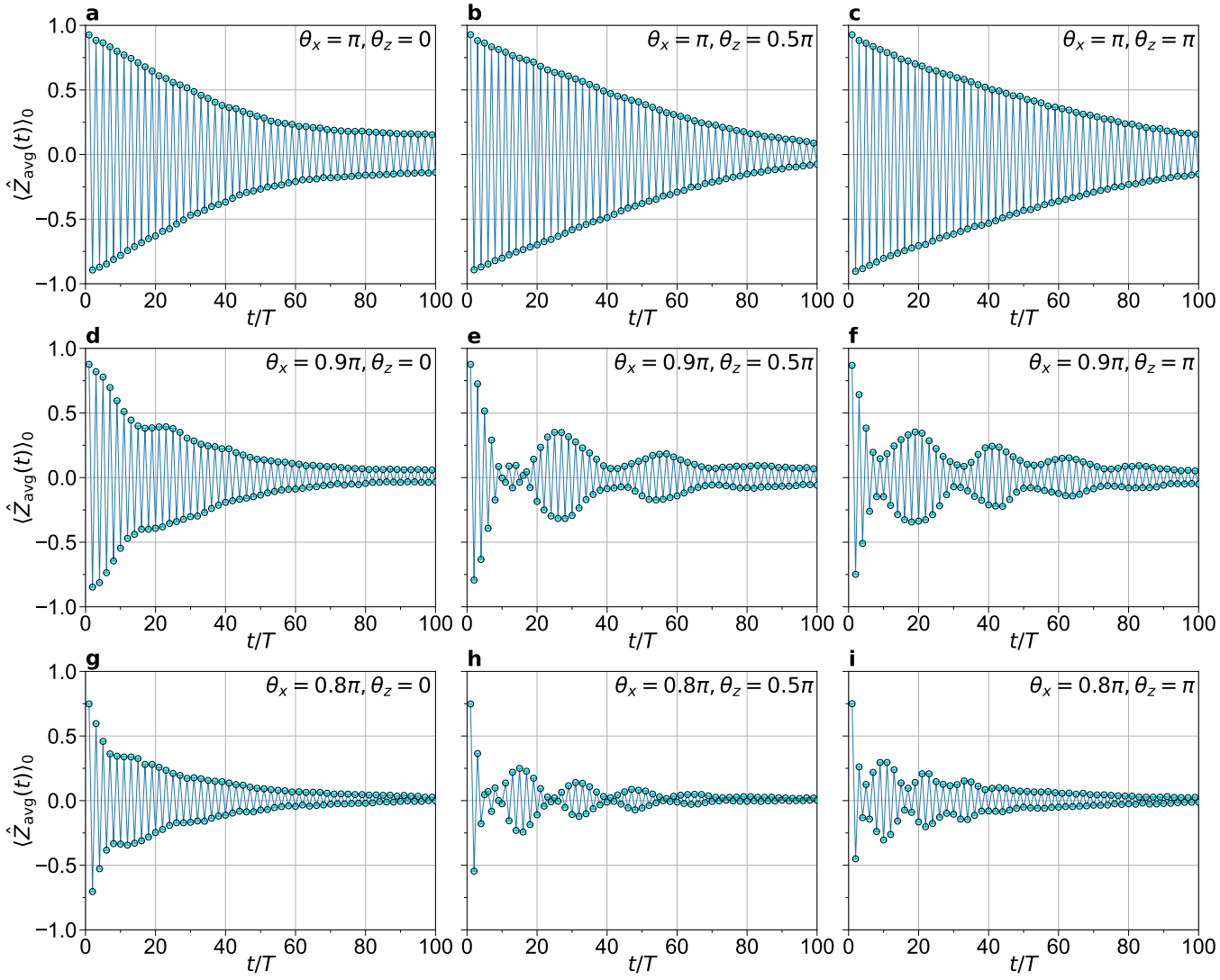

Supplementary Figure 1: Error-unmitigated raw data $\langle \hat{Z}_{\rm avg}(t) \rangle_0$ for the heavy hexagonal lattice of $L = 28$ qubits obtained using ibm_torino (see Fig. 4a). The parameters (θ_x, θ_z) are **a** $(\pi, 0)$, **b** $(\pi, 0.5\pi)$, **c** (π, π), **d** $(0.9\pi, 0)$, **e** $(0.9\pi, 0.5\pi)$, **f** $(0.9\pi, \pi)$, **g** $(0.8\pi, 0)$, **h** $(0.8\pi, 0.5\pi)$, and **i** $(0.8\pi, \pi)$. Although smaller than the size of symbols in this scale, the statistical errors of measurements are estimated in the same manner as described in the main text.

$\theta_x = 0.8\pi$, which is close to the crossover boundary between the discrete time crystal (DTC) and incommensurately modulated DTC (IM-DTC) responses and the thermalised regime, a larger χ is required to obtain the converged value, due to the increase of entanglement. For example, when $(\theta_x, \theta_z) = (0.8\pi, 0)$ (Supplementary Figure 5d), 2dTNS with $\chi = 400$ is insufficient to obtain the numerically exact results for $t \gtrsim 50$. A similar trend is observed for other parameters shown in Supplementary Figures 5e and 5f and for the MPS method shown in Supplementary Figures 4d-4f. These results suggest that the long-time time-evolution simulations of $\langle \hat{Z}_{\rm avg}(t) \rangle$ based on classical tensor network methods already face challenges even for $L = 28$ in a parameter region around $\theta_x = 0.8\pi$. We expect to encounter similar challenges for $L = 133$, where the numerically exact state-vector method cannot be applied, although a recent report suggests that the accuracy of a 2dTNS method improves as the system size increases [3]. This emphasises the significance of utilising a quantum computer precisely in this parameter regime.

III. SUPPLEMENTARY NOTE 3: RESULTS FOR A HEAVY-HEXAGONAL LATTICE OF $L = 133$ QUBITS

Supplementary Figure 6 shows the error-unmitigated raw data of the average magnetisation $\langle \hat{Z}_{\rm avg}(t) \rangle_0$ and the error-mitigated data $\langle \hat{Z}_{\rm avg}(t) \rangle$ for up to 100 time steps obtained for the $L = 133$ system using ibm_torino (see

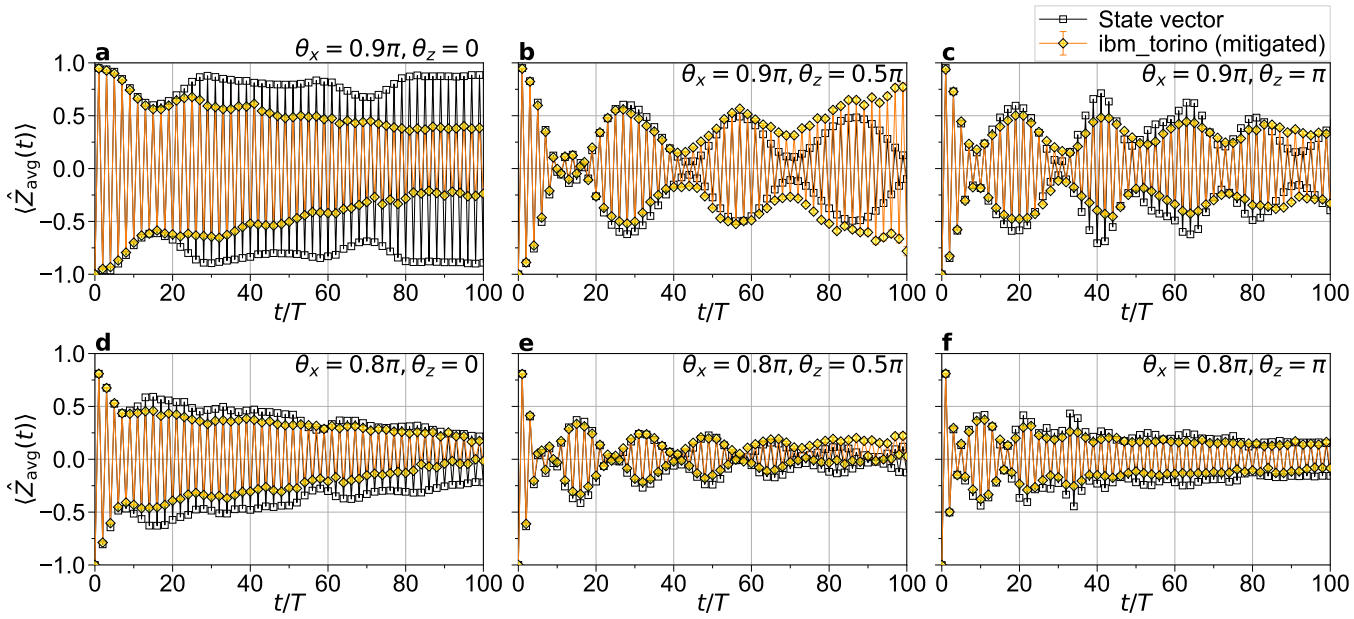

Supplementary Figure 2: Error-mitigated data $\langle \hat{Z}_{\rm avg}(t) \rangle$ (yellow diamonds) are compared with the results obtained by the classical state-vector simulations (black squares) for the heavy-hexagonal lattice of $L = 28$ qubits. The parameters (θ_x, θ_z) are **a** $(0.9\pi, 0)$, **b** $(0.9\pi, 0.5\pi)$, **c** $(0.9\pi, \pi)$, **d** $(0.8\pi, 0)$, **e** $(0.8\pi, 0.5\pi)$, and **f** $(0.8\pi, \pi)$. The error bars indicated represent the propagated error in the quantities in the numerator and the denominator of Eq. (4).

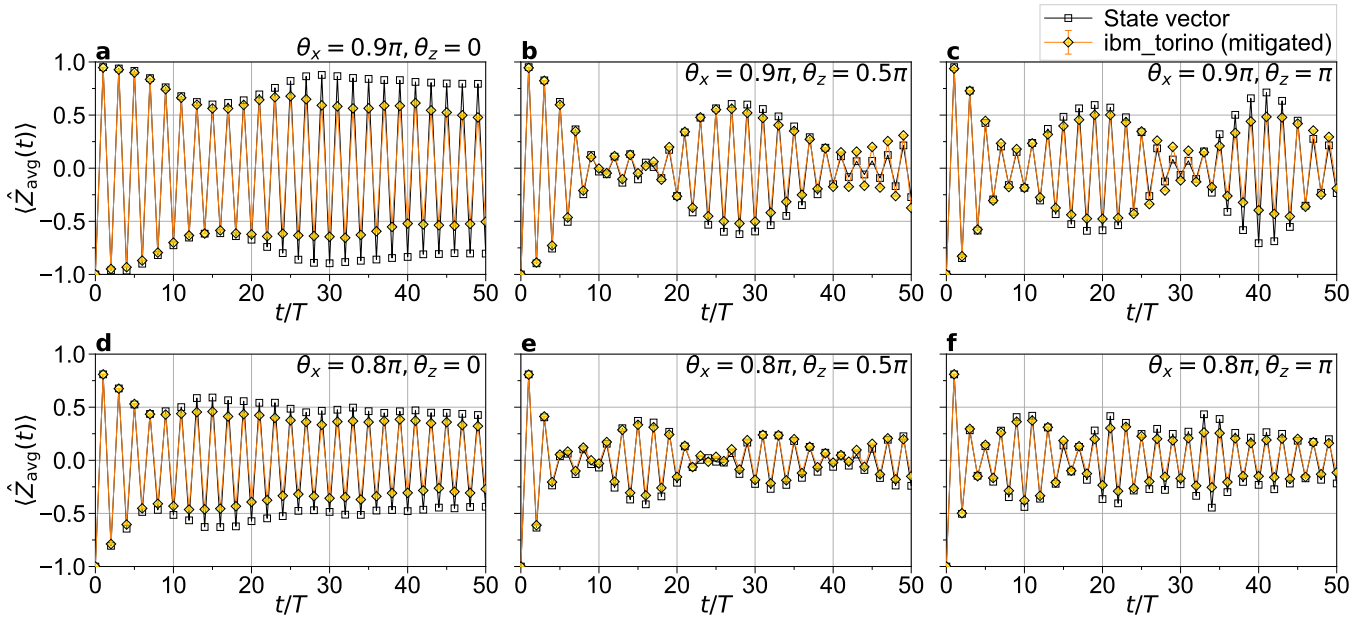

Supplementary Figure 3: Enlarged plots of Supplementary Figure 2, focusing on the time evolution for up to 50 time steps.

Fig. 4a). Here, the average is performed over the same set A of qubits as described in the main text, i.e., $A = \{57, 58, 59, 60, 61, 62, 63, 64, 65, 66, 67, 68, 69, 70, 71\}$. Remarkably, even without error mitigation, distinct signals of period-doubling oscillations persist for over 100 time steps. To mitigate errors in the raw data for $\theta_x \neq \pi$, the results corresponding to the trivial cases with $\theta_x = \pi$ are utilised, as explained in Eq. (4).

For the trivial cases with $\theta_x = \pi$, as shown in Supplementary Figures 6a-6e, $|\langle \hat{Z}_{\rm avg}(t) \rangle_0|$ should ideally be 1. However, deviations from this ideal value are observed, which become more pronounced with increasing time steps, owing to the noise and decoherence inherent in the quantum device. The number of CZ gates in the quantum circuit increases by 150 for each

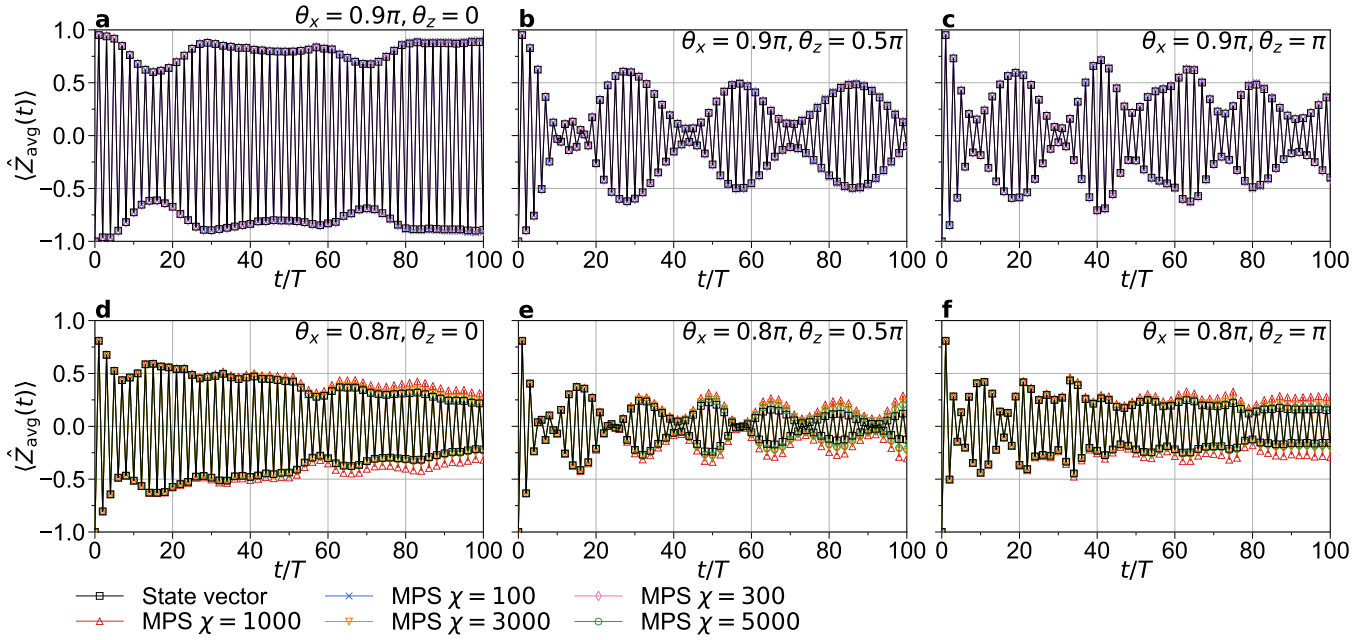

Supplementary Figure 4: Comparison of the results for $\langle \hat{Z}_{\rm avg}(t) \rangle$ on the $L = 28$ heavy-hexagonal lattice obtained by the MPS method with various bond dimensions ($\chi = 100$, 300, 1000, 3000, and 5000) and the state-vector method. The parameters (θ_x, θ_z) are **a** $(0.9\pi, 0)$, **b** $(0.9\pi, 0.5\pi)$, **c** $(0.9\pi, \pi)$, **d** $(0.8\pi, 0)$, **e** $(0.8\pi, 0.5\pi)$, and **f** $(0.8\pi, \pi)$.

operation of $\hat{U}_{\rm F}$ as defined in Eq. (2). At $t/T = 100$, the quantum circuit volume $v = 15000$ (defined by the total number of CZ gates) superficially implies $|\langle \hat{Z}_{\rm avg}(t = 100T) \rangle_0| = (1-p)^v \simeq 10^{-27}$, with a typical two-qubit infidelity in ibm_torino of $p = 4 \times 10^{-3}$. However, in practice, we observe $|\langle \hat{Z}_{\rm avg}(t = 100T) \rangle_0| \simeq 0.1$ in Supplementary Figures 6a-6e, suggesting an effective quantum circuit volume $v_{\rm eff} \simeq 600$. Since we measure local observables, $v_{\rm eff}$ is significantly smaller than v, as discussed in Ref. [4]. Additionally, it is interesting to notice that the raw data for the $L = 28$ system with the trivial parameters, as shown in Supplementary Figures 1a-1c, also exhibit $|\langle \hat{Z}_{\rm avg}(t = 100T) \rangle_0| \simeq 0.1 - 0.15$, indicating a similar $v_{\rm eff}$.

In Fig. 1d of the main text, we demonstrated that the averaged magnetisation $\langle \hat{Z}_{\rm avg}(t) \rangle$ obtained from ibm_torino with the error mitigation agrees well with those of classical 2dTNS simulations at $(\theta_x, \theta_z) = (0.8\pi, 0.5\pi)$ for the $L = 133$ system over 50 time steps. In Supplementary Figures 7 and 8, we extend this comparison to other parameters over 100 time steps. As shown in Supplementary Figures 7a-7c and 8a-8c, when $\theta_x = 0.9\pi$, the averaged magnetisation $\langle \hat{Z}_{\rm avg}(t) \rangle$ obtained by the 2dTNS method with a relatively small bond dimension $\chi = 20$ already converges sufficiently. This implies that the 2dTNS results for these parameter sets are reliable even for up to 100 time steps. Indeed, this parameter region exhibits limited entanglement growth over time steps, as indicated by the agreement between the MPS results with relatively small bond dimensions and the 2dTNS results (see Supplementary Figures 9a-9c and 10a-10c). Moreover, it is particularly remarkable that despite the simple error mitigation protocol introduced in Eq. (4) of the main text, the error-mitigated $\langle \hat{Z}_{\rm avg}(t) \rangle$ obtained from ibm_torino are in relatively good alignment with the 2dTNS results (see Supplementary Figures 7a-7c and 8a-8c).

On the other hand, as shown in Supplementary Figures 7d-7f and 8d-8f, the convergence of the 2dTNS results for $\theta_x = 0.8\pi$ is slow with increasing the bond dimension, especially for long time steps, as anticipated from the results for the $L = 28$ system shown in Supplementary Figures 5d-5f. This parameter region is close to the crossover boundary between the DTC and IM-DTC responses and the thermalised regime, where extensive entanglement growth is expected. Due to the substantial increase in entanglement, the performance of tensor-network simulations is significantly degraded, resulting in a noticeable discrepancy between MPS and 2dTNS as shown in Supplementary Figures 9d-9f and 10d-10f. Although the classical 2dTNS simulations may not have yet converged in these parameter sets for $t \gtrsim 50$, we still observe that the error-mitigated $\langle \hat{Z}_{\rm avg}(t) \rangle$ obtained from ibm_torino align well with the 2dTNS results (see Supplementary Figures 7d-7f and 8d-8f). Given that this is the parameter region where classical simulations face challenges, it underscores the value of quantum computers precisely in this parameter region.

In Supplementary Figures 11a-11f, we show the spatial distribution of the error-mitigated magnetisation $\langle \hat{Z}_j(t) \rangle$ at $t/T = 2$, 16, 24, 32, and 40, obtained using ibm_torino for the $L = 133$ system with the parameter $(\theta_x, \theta_z) = (0.9\pi, 0.5\pi)$. Here, the same error mitigation protocol as defined in Eq. (4) of the main text is employed, except that the denominator on the right hand side of Eq. (4) is replaced by the spatial average of the magnetisation over the entire system. These results are compared with those obtained using the MPS method in Supplementary Figures 11g-11l. The initial state $|\psi(0)\rangle$ is prepared as a product state with all

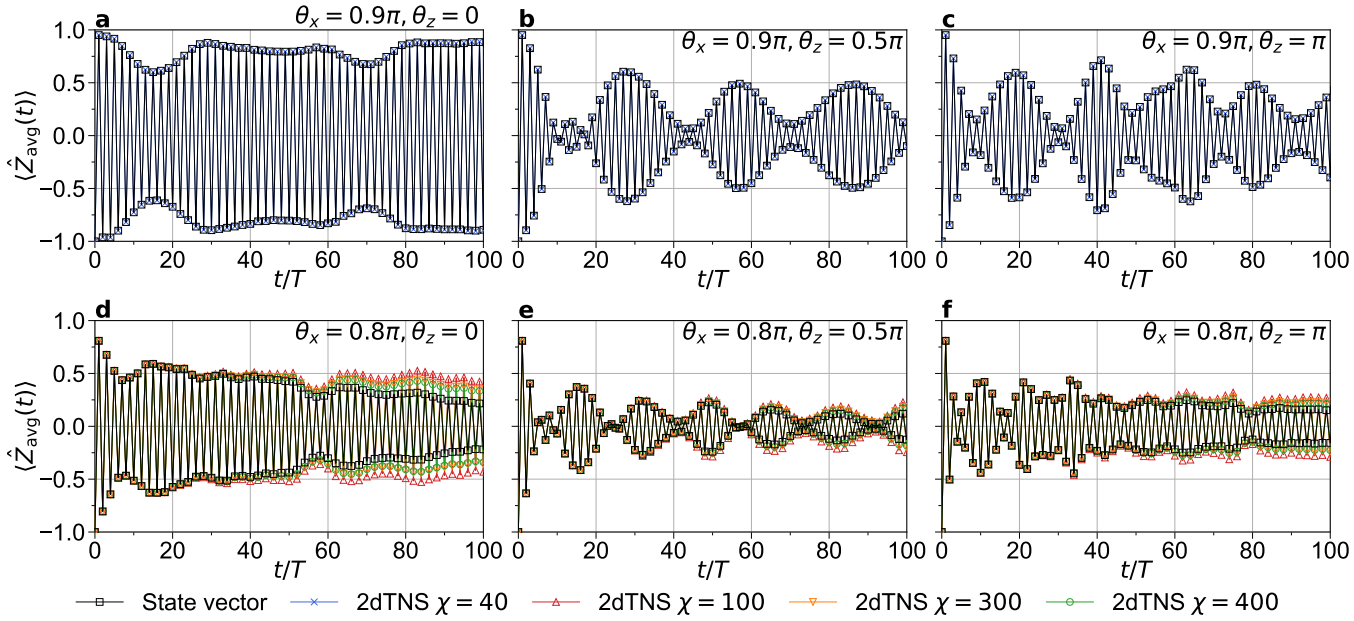

Supplementary Figure 5: Comparison of the results for $\langle \hat{Z}_{\rm avg}(t) \rangle$ on the $L = 28$ heavy-hexagonal lattice obtained by the 2dTNS method with various bond dimensions ($\chi = 40$, 100, 300, and 400) and the state-vector method. The parameters (θ_x, θ_z) are **a** $(0.9\pi, 0)$, **b** $(0.9\pi, 0.5\pi)$, **c** $(0.9\pi, \pi)$, **d** $(0.8\pi, 0)$, **e** $(0.8\pi, 0.5\pi)$, and **f** $(0.8\pi, \pi)$.

qubits set to $|0\rangle$, representing a fully polarised state. As shown in Supplementary Figure 12c, we also observe a longer-period oscillation in the averaged magnetisation $\langle \hat{Z}_{\rm avg}(t) \rangle$ upon introducing non-zero θ_z, indicating an IM-DTC response, despite the initial state differing from that used elsewhere in this study. Interestingly, the period of this oscillation closely resembles that observed in Supplementary Figures 7b and 8b, where the initial state is set differently. Furthermore, we find in Supplementary Figure 12c that the error-mitigated data are in good agreement with the results of MPS over 40-time steps.

Now, it is interesting to investigate the nature of the time-evolved state at characteristic times. As shown in Supplementary Figure 12c, the nodes of the longer-period oscillation occur at $t/T \simeq 14$ and slightly beyond 40, which are similar to those observed in Supplementary Figure 8b. At times near these nodes, specifically $t/T = 16$ and 40 as shown in Supplementary Figures 11i and 11l, respectively, we observe that the time-evolved state $|\psi(t)\rangle$ exhibits a Neel-like structure in the MPS simulations. Even in ibm_torino, we observe, at least partially, a similar Neel-like structure, as shown in Supplementary Figures 11c and 11f. Conversely, at times near the antinodes, such as $t/T = 2$, 24, and 32 shown in Supplementary Figures 11g, 11j, and 11k, respectively, the time-evolved state $|\psi(t)\rangle$ exhibits a ferromagnetic (FM)-like structure in the MPS simulations. Similarly, in ibm_torino, we observe a comparable FM-like structure, albeit partially, as shown in Supplementary Figures 11a, 11d, and 11e.

IV. SUPPLEMENTARY NOTE 4: RESULTS FOR A ONE-DIMENSIONAL LATTICE OF $L = 112$ QUBITS

While the emergence of a DTC in a one-dimensional system with short-range interactions necessitates many-body localisation, exploring the one-dimensional case driven by the same Floquet operator $\hat{U}_{\rm F}$ in Eq. (2) remains valuable. This investigation serves to highlight differences from the two-dimensional case examined throughout this paper and allows for further assessment of the reliability of results obtained using ibm_torino, along with the error-mitigation protocol introduced in Eq. (4).

A one-dimensional lattice of $L = 112$ qubits can be incorporated into the heavy-hexagonal lattice geometry of the IBM Heron processor, ibm_torino, as depicted in Supplementary Figure 13. In this configuration, qubits constituting the one-dimensional lattice are interconnected by red and blue edges. The two-qubit $\hat{R}_{Z_iZ_j}(\theta_J)$ gates in the single-cycle Floquet operator $\hat{U}_{\rm F}$ are applied on red or blue bonds concurrently in the quantum circuit. The initial state $|\psi(0)\rangle$ for the time evolution is prepared as a product state, forming a domain-wall configuration of $|0\rangle$'s and $|1\rangle$'s, represented by white and black circles, respectively, in Supplementary Figure 13. We evaluate the time evolution of the averaged magnetisation $\hat{Z}_{\rm avg}(t)$, defined in Eq. (3), over the same set A of qubits as in the heavy-hexagonal lattice of $L = 133$ qubits, i.e., $A = \{57, 58, 59, 60, 61, 62, 63, 64, 65, 66, 67, 68, 69, 70, 71\}$ (the qubit labels are indicated in Supplementary Figure 13).

Supplementary Figures 14b and 14c show the error-unmitigated raw data $\langle \hat{Z}_{\rm avg}(t) \rangle_0$ obtained using ibm_torino for the one-dimensional system of $L = 112$ qubits with the parameters $(\theta_x, \theta_z) = (0.9\pi, 0.5\pi)$ and $(0.8\pi, 0.5\pi)$, respectively. Additionally, Supplementary Figure 14a shows the error-unmitigated raw data $\langle \hat{Z}_{\rm avg}(t) \rangle_0$ for the same system but with $(\theta_x, \theta_z) = (\pi, 0.5\pi)$, which

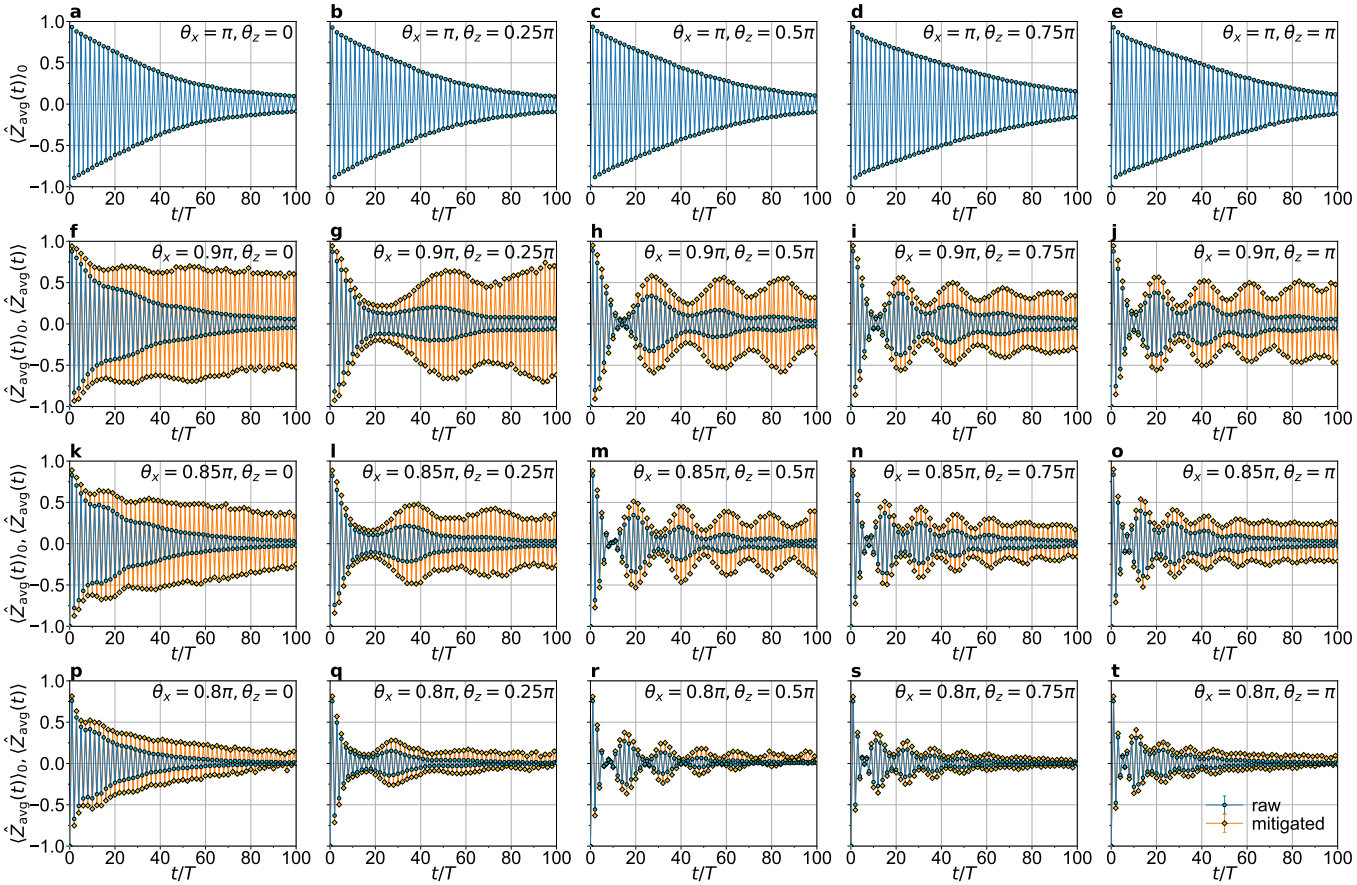

Supplementary Figure 6: Error-unmitigated raw data $\langle \hat{Z}_{\rm avg}(t)\rangle_0$ (cyan circles) and error-mitigated data $\langle \hat{Z}_{\rm avg}(t)\rangle$ (yellow diamonds) for the heavy-hexagonal lattice of $L = 133$ qubits obtained using ibm_torino (see Fig. 4a). The parameters (θ_x, θ_z) are **a** $(\pi, 0)$, **b** $(\pi, 0.25\pi)$, **c** $(\pi, 0.5\pi)$, **d** $(\pi, 0.75\pi)$, **e** (π, π), **f** $(0.9\pi, 0)$, **g** $(0.9\pi, 0.25\pi)$, **h** $(0.9\pi, 0.5\pi)$, **i** $(0.9\pi, 0.75\pi)$, **j** $(0.9\pi, \pi)$, **k** $(0.85\pi, 0)$, **l** $(0.85\pi, 0.25\pi)$, **m** $(0.85\pi, 0.5\pi)$, **n** $(0.85\pi, 0.75\pi)$, **o** $(0.85\pi, \pi)$, **p** $(0.8\pi, 0)$, **q** $(0.8\pi, 0.25\pi)$, **r** $(0.8\pi, 0.5\pi)$, **s** $(0.8\pi, 0.75\pi)$, and **t** $(0.8\pi, \pi)$. The error-mitigated data for the cases of $\theta_x = \pi$ are not shown because they are $\langle \hat{Z}_{\rm avg}(t)\rangle = \pm 1$ by definition.

are utilised to mitigate errors for $\langle \hat{Z}_{\rm avg}(t)\rangle_0$ with $(\theta_x, \theta_z) = (0.9\pi, 0.5\pi)$ and $(0.8\pi, 0.5\pi)$ shown in Supplementary Figures 14b and 14c, respectively. From the value of $|\langle \hat{Z}_{\rm avg}(t = 80T)\rangle_0|$ shown in Supplementary Figure 14a, we can estimate the effective quantum circuit volume $v_{\rm eff} \simeq 350$ at $t/T = 80$, which is significantly smaller than the quantum circuit volume $v = 8880$ (the number of CZ gates in the quantum circuit increases by 111 for each operation of $\hat{U}_{\rm F}$ in the one-dimensional system).

The error-mitigated data $\langle \hat{Z}_{\rm avg}(t)\rangle$ for the one-dimensional system of $L = 112$ qubits with the parameters $(\theta_x, \theta_z) = (0.9\pi, 0.5\pi)$ and $(0.8\pi, 0.5\pi)$ are shown in Supplementary Figure 15. In sharp contrast to the case for the heavy-hexagonal lattice of $L = 133$ qubits, the period-doubling oscillations observed in the one-dimensional system are much weaker against the deviation of θ_x from π. We find that the signals with these oscillations decay rather quickly in time steps for other parameter sets of (θ_x, θ_z) in one dimension, even when $\theta_z = 0.9$. These observations are consistent with the expectation that, in one dimension with short-range interactions and without disorder, neither a long-lived DTC nor an IM-DTC response is stabilised.

Moreover, in Supplementary Figure 15, the results for $\langle \hat{Z}_{\rm avg}(t)\rangle$ obtained using ibm_torino are compared with those calculated by the MPS method with the bond dimensions $\chi = 500$ and 1000, exhibiting the converged values. Remarkably, despite the simplicity of the error-mitigation protocol introduced, these two results obtained using ibm_torino and the MPS method show excellent agreement, confirming the reliability of the results obtained using ibm_torino.

V. SUPPLEMENTARY NOTE 5: THE ROLE OF ISING INTERACTION

In this section, we demonstrate that the Ising interaction J plays an important role in stabilising DTCs. Supplementary Figure 16 shows the averaged magnetisation $\langle \hat{Z}_{\rm avg}(t)\rangle$ with different values of θ_J and θ_x, setting $\theta_z = 0$, for the heavy-hexagonal

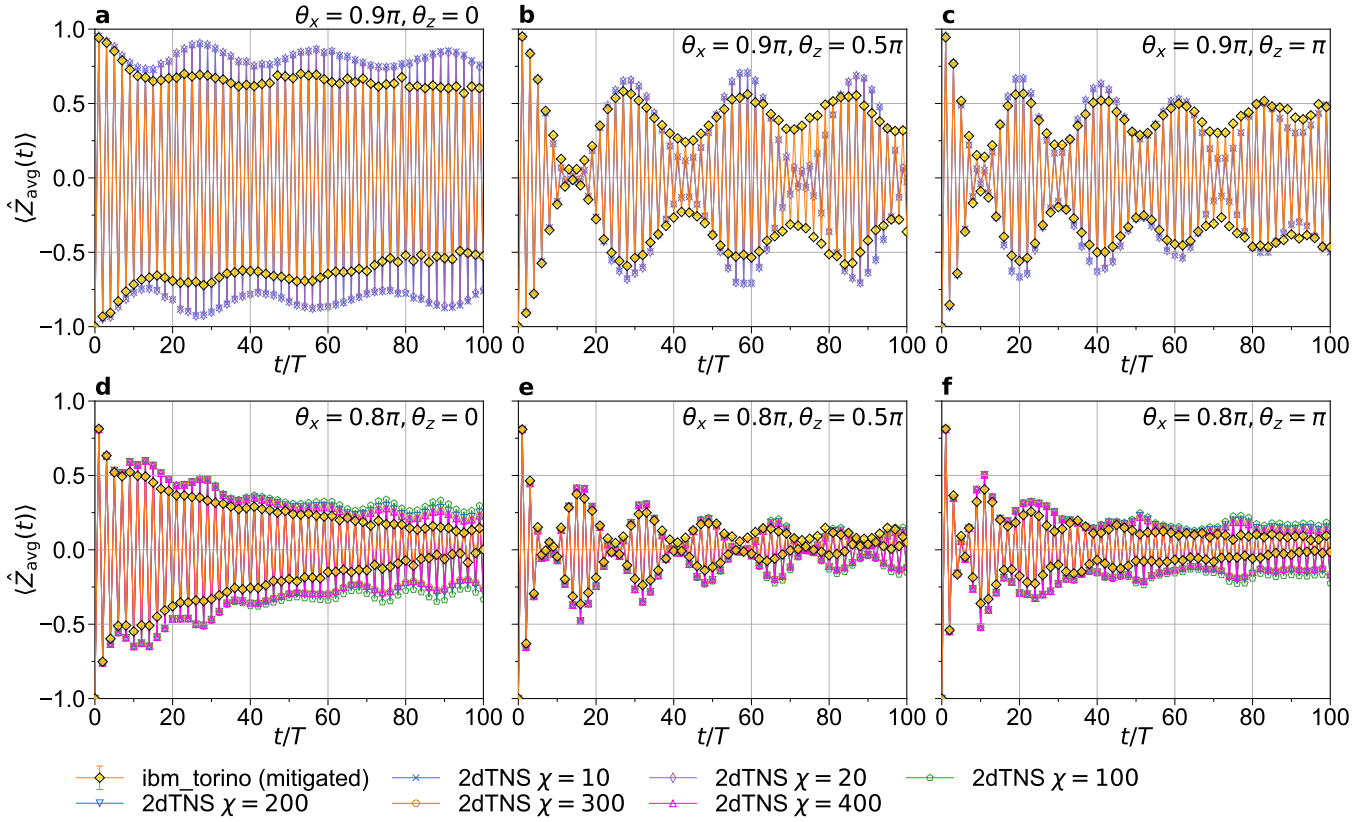

Supplementary Figure 7: Error-mitigated data $\langle \hat{Z}_{\rm avg}(t) \rangle$ are compared with the results obtained by the 2dTNS method with various bond dimensions (χ = 10, 20, 100, 200, 300, and 400) for the heavy-hexagonal lattice of $L = 133$ qubits. The parameters (θ_x, θ_z) are **a** $(0.9\pi, 0)$, **b** $(0.9\pi, 0.5\pi)$, **c** $(0.9\pi, \pi)$, **d** $(0.8\pi, 0)$, **e** $(0.8\pi, 0.5\pi)$, and **f** $(0.8\pi, \pi)$.

lattice of $L = 28$ qubits (see Fig. 4a), obtained using the state-vector method. Here, we initialise the state $|\psi(0)\rangle$ as a product state with all qubits set to $|0\rangle$ and the magnetisation $\langle \hat{Z}_{\rm avg}(t) \rangle$ is averaged over all qubits. We find that the period-doubling oscillations are quite stable at $\theta_J = -0.5\pi$, which is the parameter used in all other cases of this paper and where the DTC and IM-DTC signals are also clearly observed experimentally in ibm_torino. In contrast, for small θ_J, magnetisation oscillations are fragile against the deviation of θ_x from π, leading to a rapid decay of oscillations. This behavior indicates that the DTCs observed on the heavy-hexagonal lattice are supported by strong interactions and are realised within a finite-frequency regime.

VI. SUPPLEMENTARY NOTE 6: ERROR MITIGATION BASED ON A GLOBAL DEPOLARIZING NOISE MODEL

In this section, we provide a detailed description of our error mitigation protocol. When a qubit is depolarised into a fully mixed state $I/2$ with probability p, the depolarising noise channel modifies the qubit's density matrix ρ as [5]

$$\rho \to \mathcal{E}(\rho) = (1-p)\rho + p(I/2). \tag{1}$$

Accordingly, in an L-qubit system, the expectation value of the i-th qubit, $\langle \hat{Z}_i(t) \rangle_{\rm dp}$, under depolarizing noise is given by

$$\langle \hat{Z}_i(t) \rangle_{\rm dp} \simeq e^{-tp_i} \langle \hat{Z}_i(t) \rangle, \tag{2}$$

where p_i is the depolarising probability for the i-th qubit and $\langle \hat{Z}_i(t) \rangle$ represents the magnetisation without quantum noise. The averaged expectation value defined in Eq. (3) of the main text reads

$$\langle \hat{Z}_{\rm avg}(t) \rangle_{\rm dp} = \frac{1}{|A|} \sum_{j \in A} e^{-tp_j} \langle \hat{Z}_j(t) \rangle \tag{3}$$

$$\simeq \int dp f(p) e^{-tp} \langle \hat{Z}_{\rm avg}(t) \rangle, \tag{4}$$

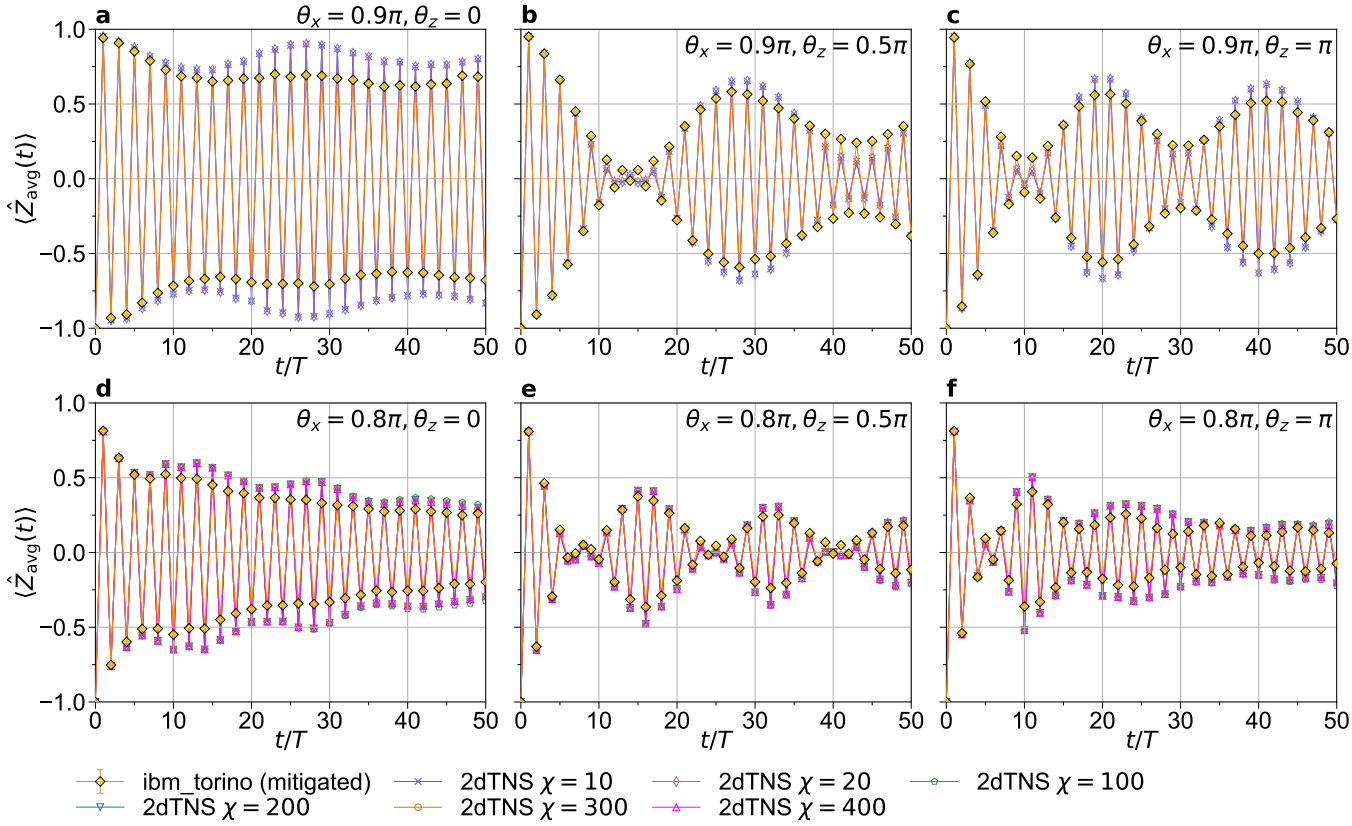

Supplementary Figure 8: Enlarged plots of Supplementary Figure 7, focusing on the time evolution for up to 50 time steps.

where, in the second line, we have introduced a probability density function $f(p)$ to approximate the discrete sum. This approximation assumes a sufficiently large system size and averaging over a large number of qubits. Under these conditions, it is expected that $\langle \hat{Z}_j \rangle$ does not depend strongly on each qubit. Assuming a Gaussian distribution $f(p) = \frac{1}{\sqrt{2\pi}\sigma} \exp\left[-\frac{(p-p_0)^2}{2\sigma^2}\right]$ with mean p_0 and variance σ^2, we obtain $\langle \hat{Z}_{\rm avg}(t) \rangle_{\rm dp} \simeq e^{-tp_0} \langle \hat{Z}_{\rm avg}(t) \rangle$. Here, in this study, we adopt a global depolarising noise model, where the depolarisation probability p is nearly uniform across qubits, implying $\sigma \sim 0$. In the following, we argue that this assumption is reasonable under the unitary circuit of the kicked Ising model.

In Supplementary Figure 17, we present the depolarisation probability p_i for each qubit on ibm_torino, estimated for the kicked Ising model on the heavy-hexagonal lattice of $L = 133$ qubits. To estimate p_i, we fit the function $e^{-tp_i} \langle \hat{Z}_i(t) \rangle$ to the experimental data $\langle \hat{Z}_i(t) \rangle_{\rm dp}$, based on Eq. (2). Here, we use the 2dTNS simulation results for the noise-free magnetisation $\langle \hat{Z}_i(t) \rangle$ on the right-hand side of Eq. (2), and the raw experimental data obtained from ibm_torino for $\langle \hat{Z}_i(t) \rangle_{\rm dp}$ on the left-hand side. The experiment was executed on July 29, 2024. Except for several noisy qubits, the values of p_i exhibit only weak dependence on the qubit index. This behavior is also reflected in the histograms showing the distribution of p_i values. As seen in Supplementary Figures 17d–17f, it is therefore reasonable to approximate the depolarising probabilities by a qubit-independent value p_0.

To further justify our error mitigation protocol based on the global depolarizing noise model, we perform state-vector simulations for the heavy-hexagonal lattice of $L = 28$ qubits. In these simulations, quantum noise is incorporated by applying one- and two-qubit depolarising channels to the system's density matrix ρ as [5, 6]

$$\mathcal{E}_i^{(1q)}(\rho) = (1 - p_1)\rho + \frac{p_1}{3} \sum_{\alpha \neq 0} \sigma_{\alpha,i} \rho \sigma_{\alpha,i} \tag{5}$$

$$\mathcal{E}_{ij}^{(2q)}(\rho) = (1 - p_2)\rho + \frac{p_2}{15} {\sum_{\alpha,\beta}}' \sigma_{\alpha,i} \sigma_{\beta,j} \rho \sigma_{\alpha,i} \sigma_{\beta,j}, \tag{6}$$

where $\sigma_{\alpha,i}$ denotes the Pauli operators acting on qubit i, with $\sigma_{\alpha,i} = I_i$, X_i, Y_i, and Z_i for $\alpha = 0$, 1, 2, and 3, respectively, and the primed sum in Eq. (6) exclude the identity pair $(\alpha, \beta) = (0, 0)$. Each single-qubit gate acting on qubit i is followed by the channel $\mathcal{E}_i^{(1q)}$, and each two-qubit gate acting on qubits i and j is followed by $\mathcal{E}_{ij}^{(2q)}$. We assume qubit-independent noise parameters and set $p_1 = p_2/10$, which approximately matches the noise characteristics of the ibm_torino device. Under this noise model, we evaluate the time evolution of the averaged magnetisation $\langle \hat{Z}_{\rm avg}(t) \rangle$, as shown in Supplementary Figures 18 and 19 for $p_2 = 0.01$

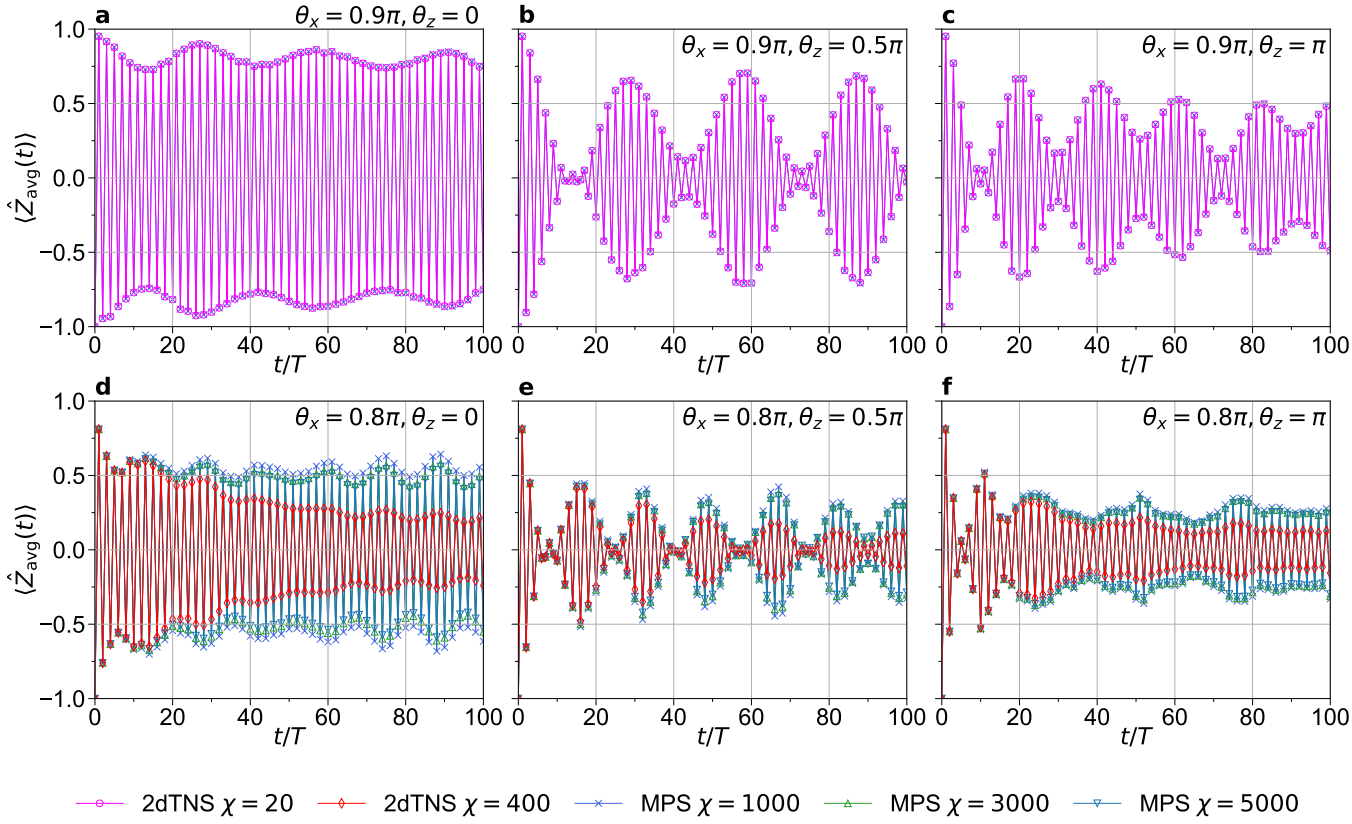

Supplementary Figure 9: Comparison of the results for $\langle \hat{Z}_{\rm avg}(t) \rangle$ on the heavy-hexagonal lattice of $L = 133$ qubits obtained by the 2dTNS method with a given bond dimension ($\chi = 20$ in panels **a**-**c** and 400 in panels **d**-**f**) and the MPS method with various bond dimensions ($\chi = 1000$, 3000, and 5000). The parameters (θ_x, θ_z) are **a** $(0.9\pi, 0)$, **b** $(0.9\pi, 0.5\pi)$, **c** $(0.9\pi, \pi)$, **d** $(0.8\pi, 0)$, **e** $(0.8\pi, 0.5\pi)$, and **f** $(0.8\pi, \pi)$.

and $p_2 = 0.005$, respectively. The same error mitigation protocol described in Eq. (4) of the main text is applied but with quantum noises generated according to the depolarising channels defined in Eqs. (5) and (6). We average over 100 independent noise realizations. More precisely, for each time step, we take sample averages over 100 noise realizations separately for the numerator and denominator in Eq. (4), using the same set of noise realizations for both. The final error-mitigated value is then obtained by taking the ratio of these sample-averaged quantities. Comparing Supplementary Figures 18 and 19 with Supplementary Figure 2, we find that $p_2 = 0.01$ is too large to accurately characterise the quantum noises in ibm_torino. On the other hand, the behavior of $\langle \hat{Z}_{\rm avg}(t) \rangle$ obtained with $p_2 = 0.005$ (see Supplementary Figure 19) closely resembles that observed in the experimental results (see Supplementary Figure 2), at least for $t/T < 50$. Note that the average error rate of CZ gate on ibm_torino is approximately 0.006.

From the above discussions, we conclude that the global depolarising noise model provides an effective description of quantum noise in the observation of $\langle \hat{Z}_{\rm avg}(t) \rangle$ for the kicked Ising model. The effectiveness of this model for mitigating quantum noise has also been pointed out in Ref. [7]. In quantum simulations of the kicked Ising model with large system size L, the number of gates per circuit layer becomes substantial, making the depolarising noise model a suitable effective approximation for characterising the accumulated noise.

The depolarising noise model is based on the simplifying assumption that all types of Pauli errors act equivalently. This is one reason why it is often justified in random unitary circuits and/or the deep regions of unitary circuits. In the kicked Ising model, particularly for $\theta_x \sim \pi$, the effect of the depolarising noise defined in Eq. (6) is expected to be anisotropic, assuming that the initial state $|\psi(0)\rangle$ is prepared as a product state in the computational basis. This is because phase-flip errors (Z-type) lead to a smaller decay in $\langle \hat{Z}_{\rm avg}(t) \rangle_0$ than bit-flip errors (X- or Y-type) [6]. Assuming that phase-flip errors have no effect, i.e., $\rho = I_i Z_j \rho I_i Z_j = Z_i I_j \rho Z_i I_j = Z_i Z_j \rho Z_i Z_j$, the two-qubit depolarising channel in Eq. (6) can be modified as

$$\tilde{\mathcal{E}}_{ij}^{(2q)}(\rho) = \left(1 - \frac{4}{5} p_2\right) \rho + \frac{p_2}{15} \sum\nolimits'_{\alpha,\beta} \sigma_{\alpha,i} \sigma_{\beta,j} \rho \sigma_{\alpha,i} \sigma_{\beta,j}, \tag{7}$$

which results in a reduced fidelity $\tilde{f} := 1 - 4p_2/5 \sim f^{4/5}$, where $f = 1 - p_2$. To correct the underestimated fidelity at $\theta_x = \pi$, we

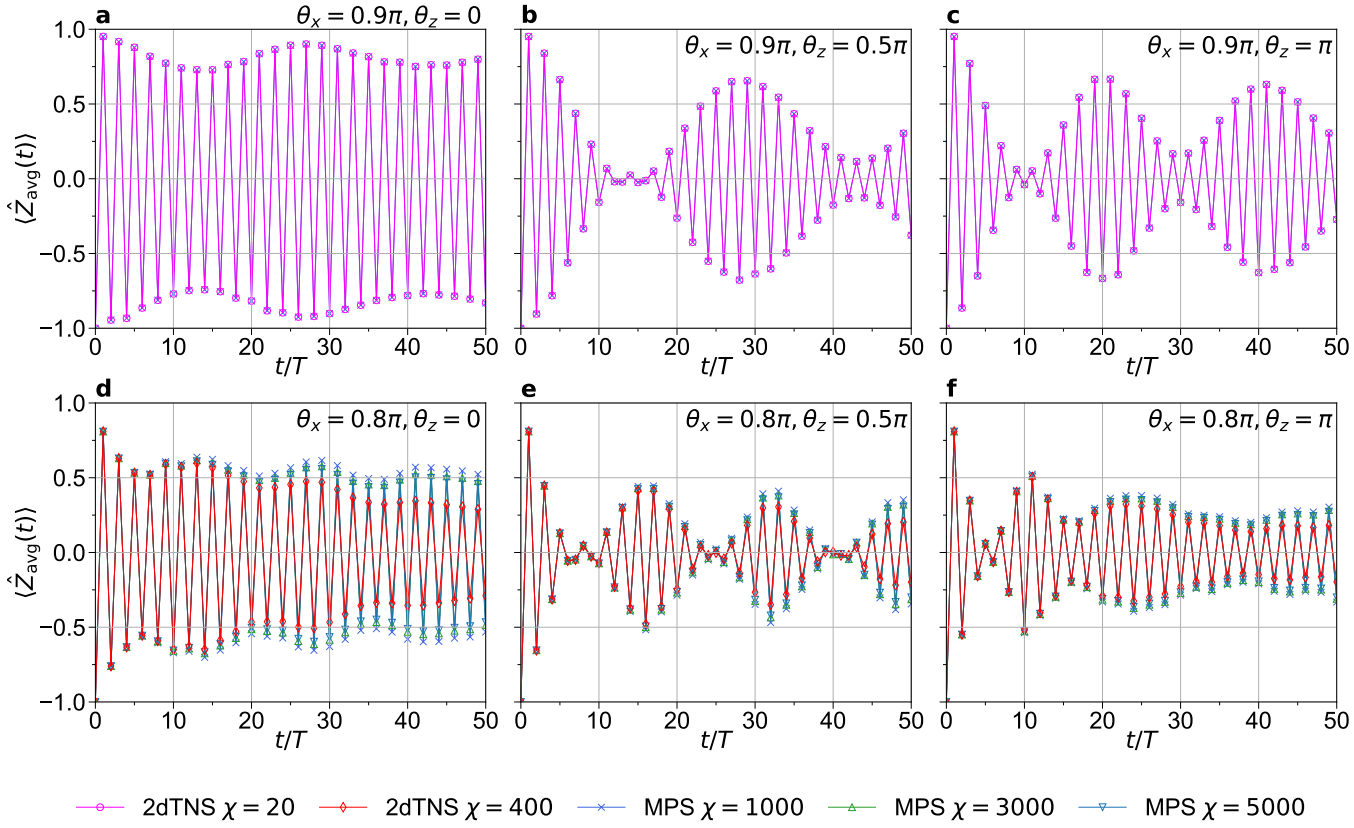

Supplementary Figure 10: Enlarged plots of Supplementary Figure 9, focusing on the time evolution for up to 50 time steps.

can propose the following modification to the error mitigation formula [Eq. (4) in the main text]:

$$\langle \hat{Z}_{\mathrm{avg}}(t) \rangle \approx \frac{\langle \hat{Z}_{\mathrm{avg}}(t) \rangle_0}{|\langle \hat{Z}_{\mathrm{avg}}(t) \rangle_{0,\theta_x=\pi}|^{5/4}}. \tag{8}$$

In this correction, we neglect single-qubit errors, whose probability p_1 is smaller than p_2. Supplementary Figure 20 shows $\langle \hat{Z}_{\mathrm{avg}}(t) \rangle$ obtained using the modified error mitigation protocol based on Eq. (8). Comparing to the mitigation using Eq. (4) [see Supplementary Figure 8], the modified protocol yields slightly better agreement with the 2dTNS results, suggesting that accounting for the anisotropy of Pauli errors can improve mitigation accuracy.

VII. SUPPLEMENTARY NOTE 7: OUT-OF-TIME-ORDER CORRELATORS

In this section, we demonstrate that the DTCs observed in the kicked Ising model on a heavy-hexagonal lattice are realized in a prethermal regime. To this end, we perform state-vector simulations to evaluate the out-of-time-order correlator (OTOC) [8, 9], defined as $\langle \hat{X}_j(t)\hat{Z}_k\hat{X}_j(t)\hat{Z}_k \rangle$, for a system of $L = 21$ qubits arranged as shown in the inset of Supplementary Figure 21d. The results are presented in Supplementary Figures 21 and 22. The growth of local operators, i.e., quantum scrambling [10, 11], describes the spreading of quantum information in time. OTOCs are widely used as quantitative probes of such scrambling. At early times, the OTOC takes a value of 1 becuase $\hat{X}_j(t)$ and $\hat{Z}_k$ are initially nonoverlapping and thus commute. As scrambling progresses and the operators fail to commute, the OTOC decreases and eventually saturates to 0. For $\theta_x = 0.9\pi$ and 0.8π, the OTOC remains near 1 or exhibits persistent oscillations, as shown in Supplementary Figures 21a and 21b, respectively. This behavior indicates the absence of significant quantum scrambling up to $t/T < 50$. Since scrambling underpins thermalisation in isolated quantum systems [12, 13], its suppression results in the long-lived stability of the prethermal DTCs observed in this regime. In contrast, for $\theta_x = 0.7\pi$ and 0.6π, the OTOC decays and saturates to 0, as shown in Supplementary Figures 21c and 21d, signaling the onset of scrambling. The decay is faster at $\theta_x = 0.6\pi$ than at $\theta_x = 0.7\pi$, where a short-lived prethermal plateau appears around $t/T \sim 20$ (Supplementary Figure 21c). To examine the spatial dependence of scrambing, we show colormaps of

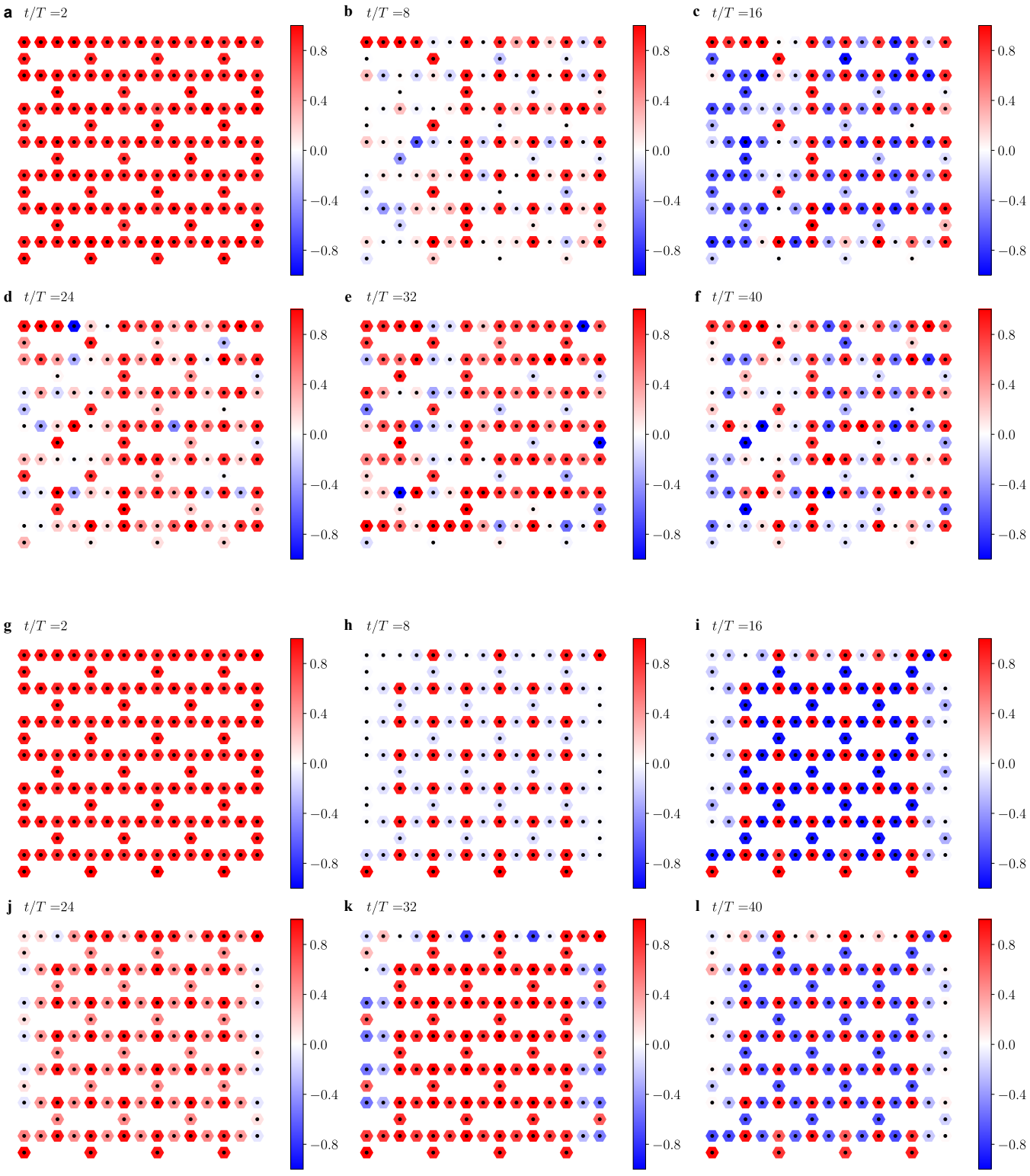

Supplementary Figure 11: Time evolution of local expectation values $\langle Z_j(t)\rangle$ at t/T = 2, 8, 16, 24, 32, and 40 on the heavy-hexagonal lattice of L = 133 qubits with the parameter $(\theta_x, \theta_z) = (0.9\pi, 0.5\pi)$. **a**-**f** Error-mitigated expectation values obtained using ibm_torino. **g**-**l** The corresponding results obtained by the MPS method with the bond dimension χ = 1000. Here, the initial state is prepared as a product state with all qubits set to $|0\rangle$, representing a fully-polarised state.

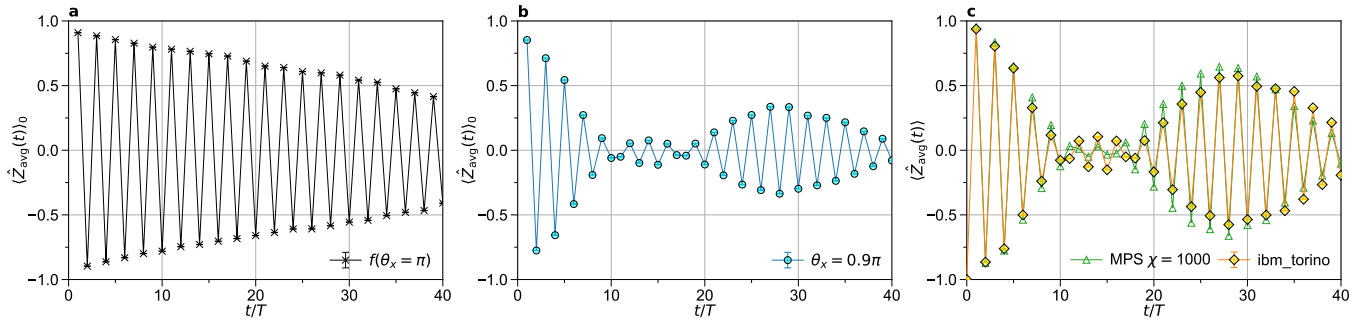

Supplementary Figure 12: **a** Raw data of the averaged magnetisation $\langle \hat{Z}_{\rm avg}(t)\rangle_{0,\theta_x=\pi}$ for the heavy-hexagonal lattice of $L = 133$ qubits with the parameter $(\theta_x, \theta_z) = (\pi, 0.5\pi)$ obtained using ibm_torino. **b** Same as **a**, but with the parameter $(\theta_x, \theta_z) = (0.9\pi, 0.5\pi)$. **c** Error-mitigated data (yellow diamonds) of the averaged magnetisation $\langle \hat{Z}_{\rm avg}(t)\rangle$ for the heavy-hexagonal lattice of $L = 133$ qubits with the parameter $(\theta_x, \theta_z) = (0.9\pi, 0.5\pi)$. The results obtained by the MPS method with the bond dimension $\chi = 1000$ are also shown with green triangles. Here, the initial state is prepared as a product state with all qubits set to $|0\rangle$, i.e., a fully-polarised state.

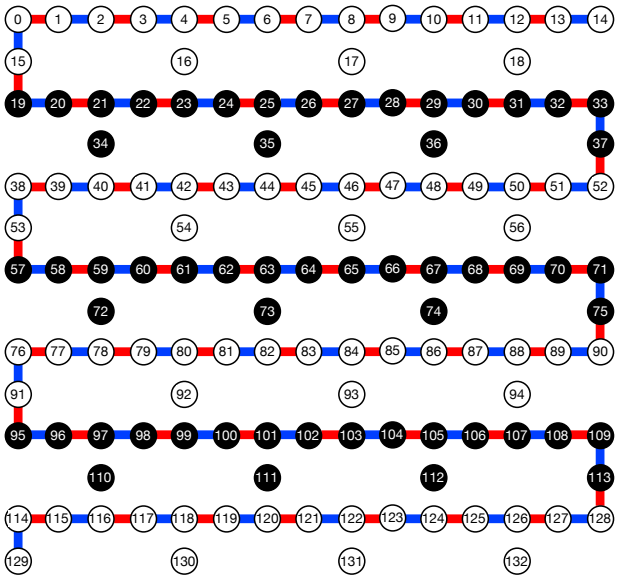

Supplementary Figure 13: A one-dimensional lattice of $L = 112$ qubits embedded in the heavy-hexagonal lattice geometry of the IBM Quantum Heron processor, ibm_torino. The qubits forming the one-dimensional lattice are connected by red and blue edges. When the quantum device is utilised, $\hat{R}_{Z_jZ_j}(\theta_J)$ gates in the single-cycle Floquet operator $\hat{U}_{\rm F}$ applied on red or blue bonds are operated in parallel. The initial state is prepared as a product state with qubits indicated by white (black) circles set to $|0\rangle$ ($|1\rangle$).

$\langle \hat{X}_j(t)\hat{Z}_{20}\hat{X}_j(t)\hat{Z}_{20}\rangle$ at various time steps in Supplementary Figure 22. The operator spreading is clearly slower for $\theta_x = 0.9\pi$ and 0.8π compared to $\theta_x = 0.7\pi$. Indeed, for $\theta_x = 0.9\pi$ and 0.8π, several qubits still exhibit OTOC values close to 1 even at $t/T = 50$.

For comparison, we also present the OTOC $\langle \hat{X}_j(t)\hat{Z}_{23}\hat{X}_j(t)\hat{Z}_{23}\rangle$ for the kicked Ising model on a square lattice of $L = 24$ qubits, arranged as shown in the inset of Supplementary Figure 23b. The results, obtained using the state-vector method, are shown in Supplementary Figures 23 and 24. We find that the OTOCs on the square lattice saturate to zero even for $\theta_x = 0.9\pi$, whereas those on the heavy-hexagonal lattice remain far from saturation under the same conditions (see Supplementary Figures 21a). This comparison highlights that quantum scrambling proceeds significantly more slowly on the heavy-hexagonal lattice, supporting the emergence of stable prethermal DTCs in this geometry. Notably, for $\theta_x = 0.9\pi$ and 0.8π, we observe a clear suppression of quantum-information propagation at qubits $j = 4$ and 16. This behaviour arises because symmetry charges accumulate at these coordination-3 qubits, effectively acting as blocking points for information flow (see Ref. [14] for details). In contrast, at $\theta_x = 0.7\pi$, the entanglement propagation overcomes these blocking sites, allowing information to spread throughout the lattice and leading to full quantum scrambling.

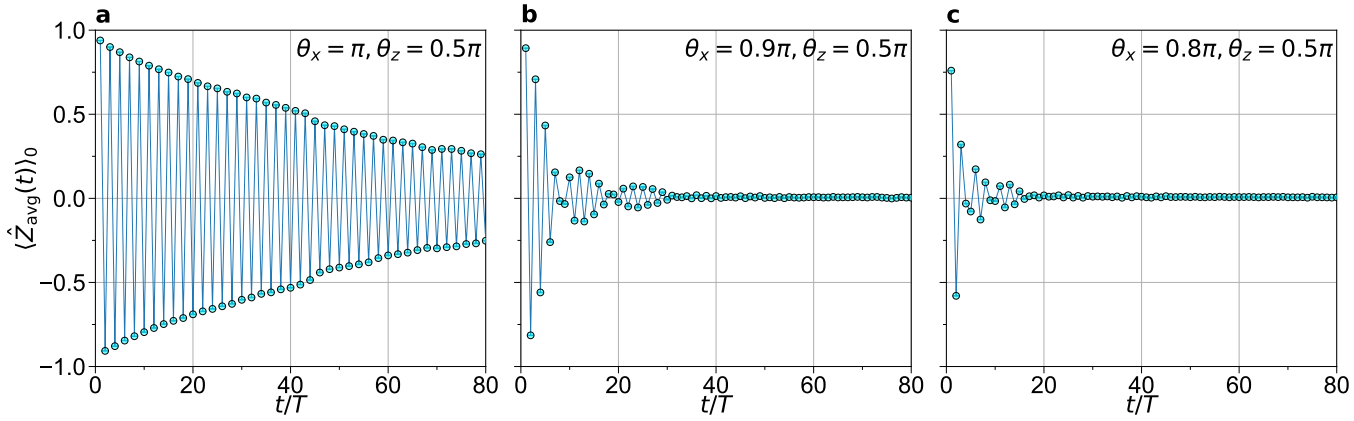

Supplementary Figure 14: Error-unmitigated raw data $\langle \hat{Z}_{\rm avg}(t) \rangle_0$ for the one-dimensional lattice of $L = 112$ qubits obtained using ibm_torino (see Supplementary Figure 13). The parameters (θ_x, θ_z) are **a** $(\pi, 0.5\pi)$, **b** $(0.9\pi, 0.5\pi)$, and **c** $(0.8\pi, 0.5\pi)$.

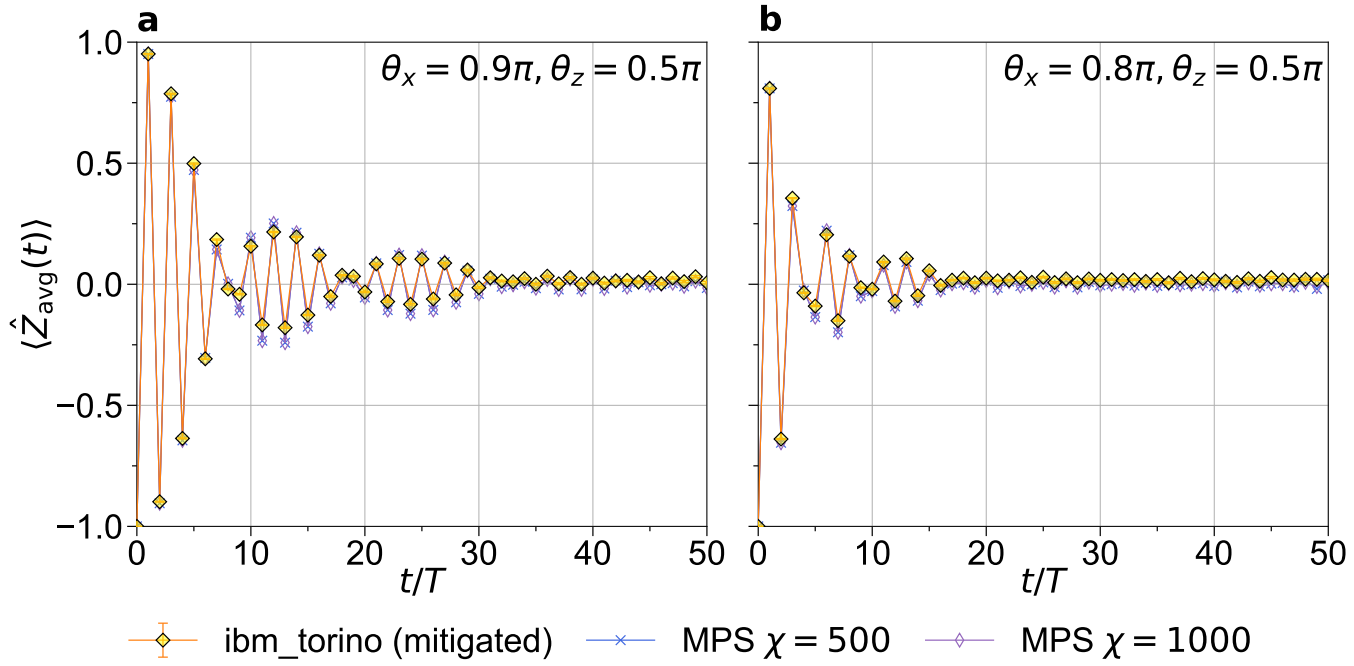

Supplementary Figure 15: Error-mitigated data $\langle \hat{Z}_{\rm avg}(t) \rangle$ (yellow diamonds) are compared with the results obtained by the MPS simulations with the bond dimensions $\chi = 500$ and 1000 (shown as blue crosses and purple diamonds, respectively) for the one-dimensional lattice of $L = 112$ qubits. The parameters (θ_x, θ_z) are **a** $(0.9\pi, 0.5\pi)$ and **b** $(0.8\pi, 0.5\pi)$.

VIII. SUPPLEMENTARY NOTE 8: LONG-TIME DYNAMICS

In this section, we present the long-time dynamics of magnetisation oscillations in the kicked Ising model on a heavy-hexagonal lattice. It is well known that Floquet systems with a small transverse field perturbation $\theta_x \sim \pi$ can exhibit two-step relaxation dynamics [15, 16]. Following an initial rapid relaxation, the system enters a metastable prethermal state characterized by slow energy absorption. Eventually, it relaxes to an infinite-temperature state, as predicted by the Floquet eigenstate thermalization hypothesis (ETH) [17, 18].

Supplementary Figures 25 and 26 show the absolute value of the magnetisation, $|\langle \hat{Z}_{\rm avg}(t) \rangle|$, averaged over the entire system, for heavy-hexagonal lattices with $L = 21$ qubits (see the inset of Supplementary Figure 25a) and $L = 28$ qubits (see the inset of Supplementary Figure 26a), respectively. These results are obtained using the state-vector method with the initial state $|\psi(0)\rangle$ prepared as a product state with all qubits seto to $|0\rangle$. For the $L = 21$ qubit system, prethermal plateau-like structures are observed in the time intervals $10 < t/T < 200$, $10 < t/T < 70$, and $10 < t/T < 30$ for $\theta_x = 0.9\pi$, 0.85π, and 0.8π, respectively.

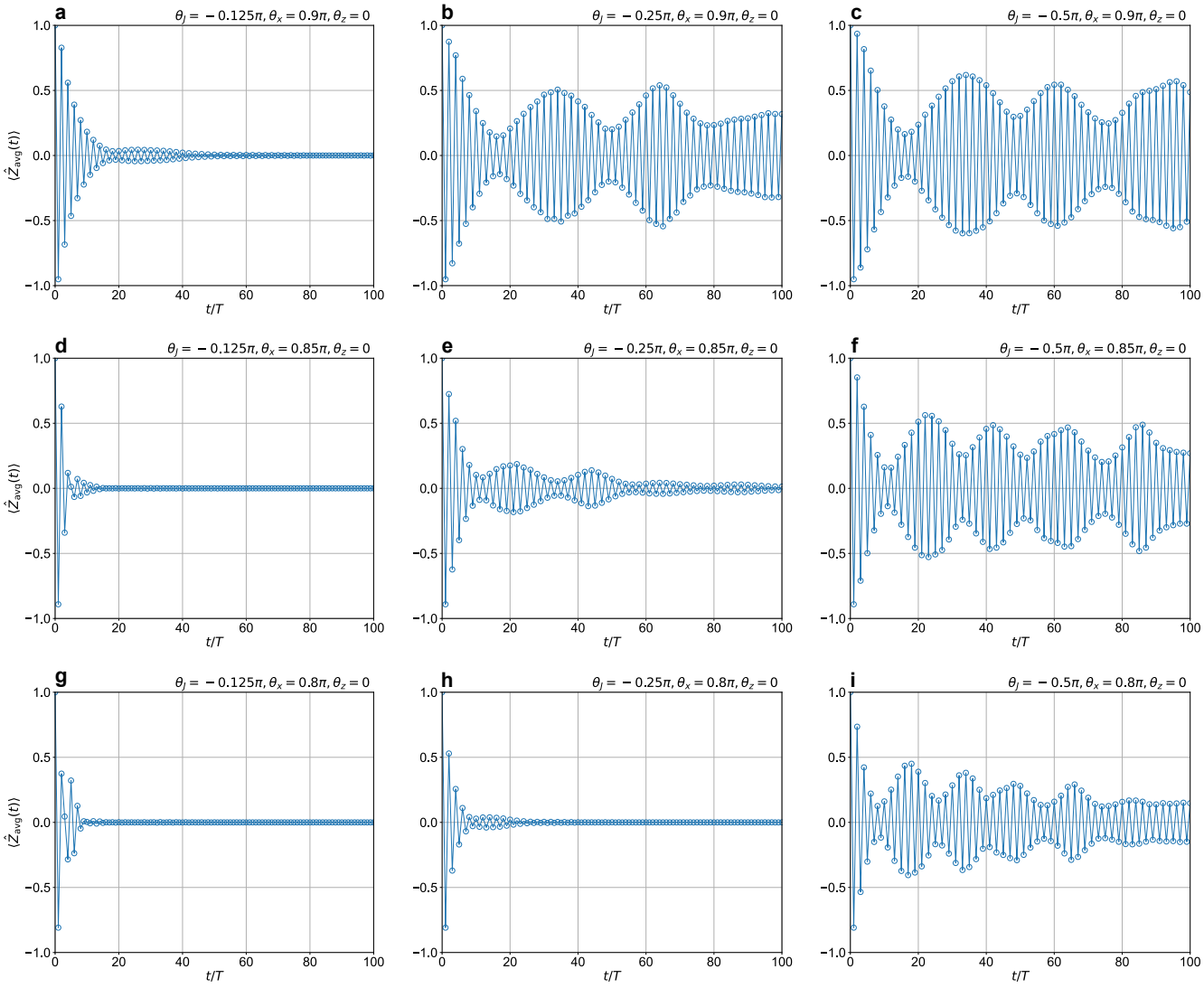

Supplementary Figure 16: Average magnetization $\langle \hat{Z}_{\mathrm{avg}}(t) \rangle$ for the heavy-hexagonal lattice of $L = 28$ qubits obtained using the state-vector method. The parameter θ_x is set to 0.9π for **a**–**c**, 0.85π for **d**–**f**, and 0.8π for **g**–**i**, while the parameter θ_z is fixed at 0. The parameter θ_J of the Ising interaction is -0.125π in **a**, **d**, and **g**, -0.25π in **b**, **e**, and **h**, and -0.5π in **c**, **f**, and **i**. Here, the initial state $|\psi(0)\rangle$ is prepared as a product state with all qubits set to $|0\rangle$, i.e., a fully-polarised state, and the magnetisation $\langle \hat{Z}_{\mathrm{avg}}(t) \rangle$ is averaged over all qubits.

These plateau structures persist for longer durations in the $L = 28$ qubit system, appearing in the intervals $10 < t/T < 1000$, $10 < t/T < 200$, and $10 < t/T < 70$ for the same values of θ_x. This system size dependence suggests that prethermal DTCs on the heavy-hexagonal lattice become increasingly robust with larger system sizes.

Together with the behavior of the OTOCs discussed in Sec. VII, these results support the conclusion that prethermal DTCs emerge in the parameter range $0.8\pi \lesssim \theta_x < \pi$ on the heavy-hexagonal lattice.

IX. SUPPLEMENTARY NOTE 9: TENSOR NETWORK SIMULATIONS: 2DTNS

In this section, we describe our 2dTNS method based on a gauging tensor network technique. Gauging tensor network states (TNSs) provide a compact representation of quantum states within an approximation framework [3, 19–28]. The gauging tensor network consists of two types of tensors: vertex tensors and gauge tensors. The vertex tensor has a physical bond representing qubit degrees of freedom, as well as virtual bonds that reflect the topology of the system. The gauge tensor is positioned on the edge connecting neighboring vertex tensors. The structure of the gauging tensor network for the IBM Quantum Heron processor,

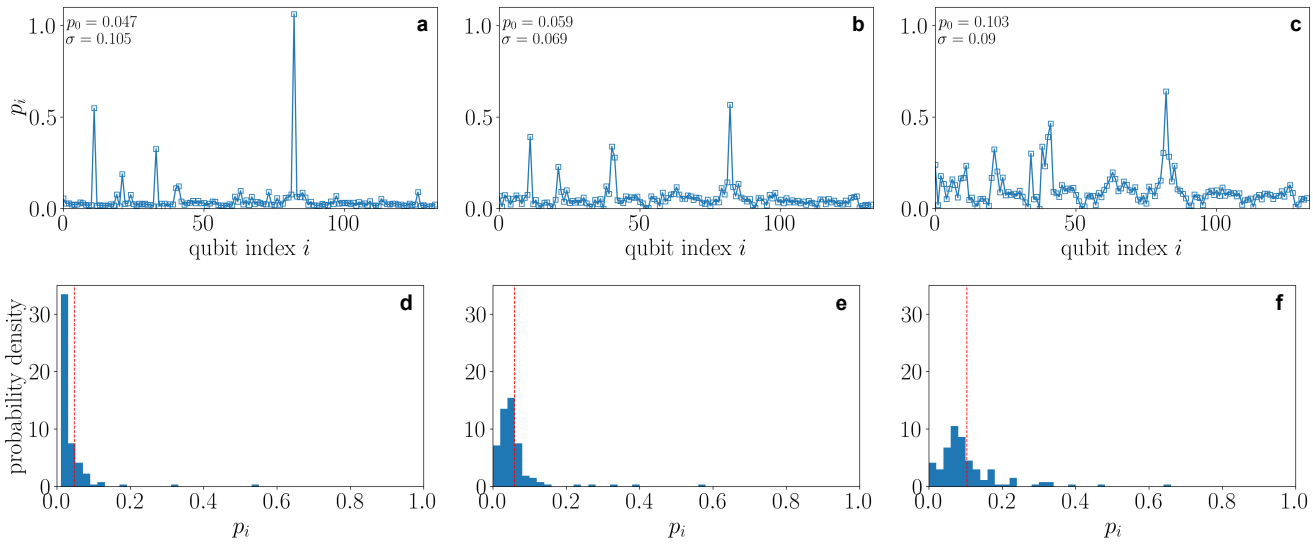

Supplementary Figure 17: Depolarisation probability p_i for each qubit on ibm_torino estimated for the kicked Ising model on the heavy-hexagonal lattice of $L = 133$ qubits. The model parameter is set to **a** $\theta_x = \pi$, **b** 0.9π, and **c** 0.8π, with θ_z fixed at zero. The corresponding values of p_0 and σ are also shown for each θ_x. Histograms of p_i are shown for **d** $\theta_x = \pi$, **e** 0.9π, and **f** 0.8π, where the red dashed lines indicate p_0.

ibm_torino, which forms the heavy-hexagonal lattice, is illustrated in Supplementary Figure 27. For the heavy-hexagonal lattice, there are two types of vertex tensors: one with two virtual bonds and the other with three virtual bonds. The dimension of the virtual bond, i.e., bond dimension χ, controls the accuracy of the approximation. In our study, χ denotes the maximum bond dimension utilised in a TNS.

To apply a two-qubit gate to a gauging TNS with bond dimension χ, we employ the time-evolving block decimation (TEBD) method [19], outlined in Supplementary Figure 28. Initially, in step (a), the surrounding gauge tensors and the vertex tensors targeted for the two-qubit gate are contracted. Following this, QR decomposition is performed on the vertex tensor in step (b) to optimise the computational efficiency for the subsequent singular value decomposition (SVD) in step (d). All tensors connected to the two-qubit gate, along with the gauge tensor, are contracted in step (c). SVD is then executed on the resulting tensor in step (d), yielding a total of 2χ singular values. To prevent an increase in bond dimension, only the χ largest singular values are retained, with the remaining space truncated to dimension χ. Subsequently, this truncated diagonal matrix, composed of the χ largest singular values, replaces the original gauge tensor, with the neighboring vertex tensors updated, in steps (e)-(g).

More generally, in a gauging TNS, gauge tensors are typically represented as diagonal matrices. While a gauging TNS can describe the same quantum state, there exist various approaches to implement the gauge at an edge. One particularly notable gauge is the canonical gauge, also known as Vidal's gauge. Within this framework of the Vidal gauge, the vertex tensors become isometric after absorbing all but one of the gauge tensors on their adjacent bonds, as schematically shown in Supplementary Figure 29(a). A notable advantage of employing the Vidal gauge is evident when computing the expectation value of a local physical quantity. For instance, when evaluating the expectation value of a physical quantity at a single site, the laborious task of contracting the entire tensor network is replaced with local tensor contraction, as shown in Supplementary Figure 29(c). This presents a significant advantage, particularly in the context of two-dimensional TNSs, where full contraction becomes computationally infeasible without resorting to approximate techniques.

However, the TEBD process generally disrupts the Vidal gauge, even when we start with a TNS with the Vidal gauge. A procedure to restore this broken gauge is known as regauging. Particularly, simple and well-known regauging methods include trivial simple update (tSU) [29–31] and belief propagation [3, 28, 32–35]. In our study, we adopt the tSU regauging method outlined in Supplementary Figure 30. The tSU is a procedure essentially equivalent to that described in Supplementary Figure 28, except that the two-qubit gate is replaced with identity. Repeatedly applying this procedure across all edges in the tensor network improves the gauge and ultimately restores the Vidal gauge, in principle. While there is a mathematical proof for this in a tree tensor network [35], it is not established for a general tensor network with a loop structure. In our case, we assess the error C from the Vidal gauge, as defined in Supplementary Figure 29(b), at each time step, and iterate the tSU until it sufficiently converges. Moreover, we observe no significant difference between taking the Vidal gauge at every time step and only before measuring a physical quantity. This suggests that the accuracy of a TNS itself at each time step is not greatly influenced by whether the Vidal gauge is taken or not. Additionally, we performed calculations using the belief propagation [3, 28], and found

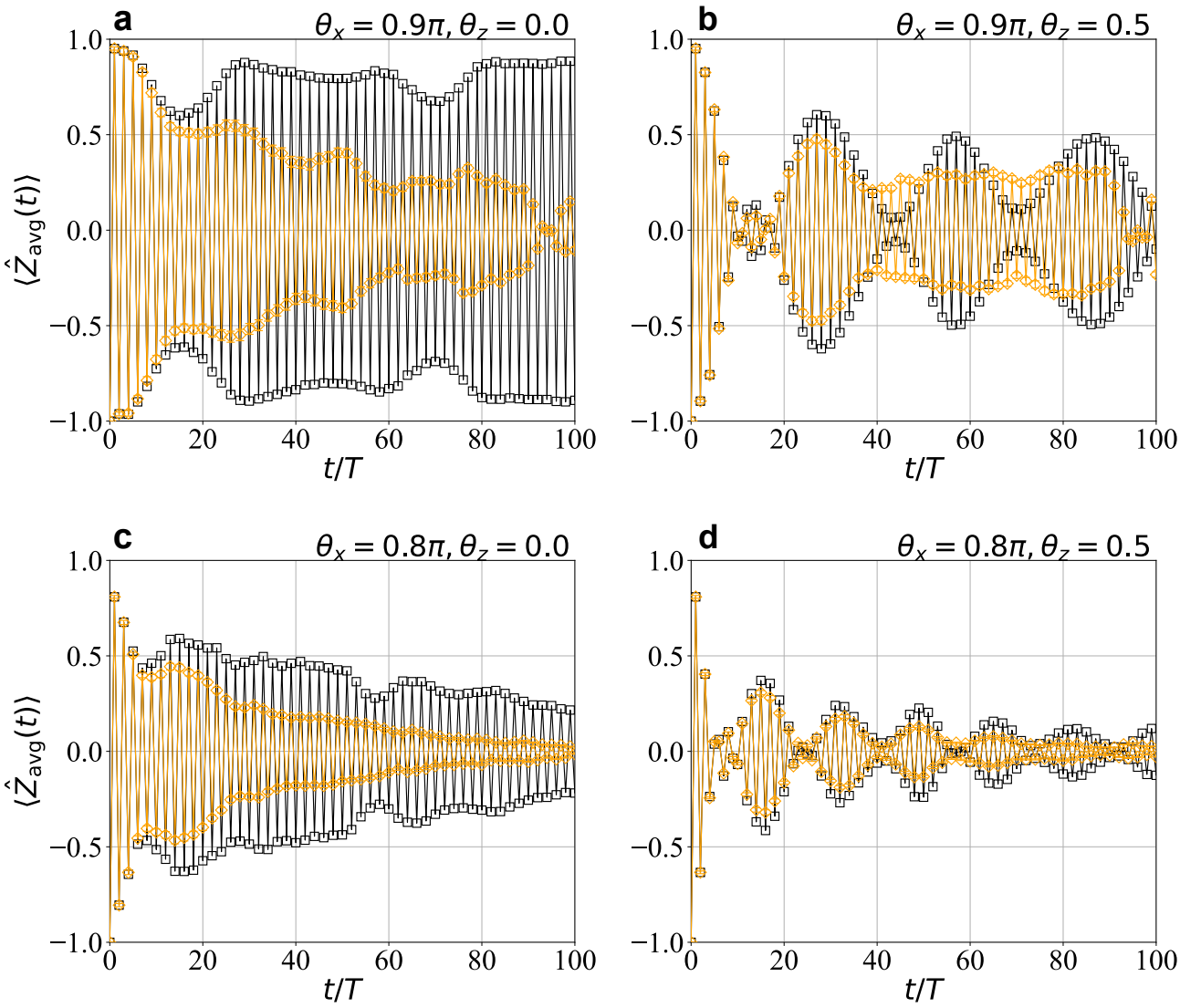

Supplementary Figure 18: Error-mitigated average magnetisation $\langle \hat{Z}_{\rm avg}(t) \rangle$ (yellow diamonds) are compared with the noise-free results (black squares), both obtained by the classical state-vector method, for the heavy-hexagonal lattice of $L = 28$ qubits. Quantum noise is introduced via the depolarising channels defined in Eqs. (5) and (6), with averages taken over 100 independent noise realizations using $p_2 = 10p_1 = 0.01$. The parameters (θ_x, θ_z) are **a** $(0.9\pi, 0)$, **b** $(0.9\pi, 0.5\pi)$, **c** $(0.8\pi, 0)$, and **d** $(0.8\pi, 0.5\pi)$. The error bars indicated represent the propagated error in the quantities in the numerator and the denominator of Eq. (4).

that the results coincide with those obtained using the tSU, indicating convergence to the same fixed point [35].

We utilise this method, referred to as the 2dTNS method, to simulate the quantum dynamics governed by the Floquet operator $\hat{U}_{\rm F}$ described in the main text. Note that the single-qubit unitary gates $\hat{R}_{Z_i}(\theta_z)$ and $\hat{R}_{X_i}(\theta_x)$ can be treated exactly within this framework. As benchmark calculations, in Supplementary Figure 5, we compare the results of $\langle \hat{Z}_{\rm avg}(t) \rangle$ for the heavy-hexagonal lattice of $L = 28$ qubits obtained by the 2dTNS method with various bond dimensions ($\chi = 40$, 100, 300, and 400) with those obtained by the state-vector method.

Finally, Supplementary Figure 31 shows typical results for the convergence of a TNS towards that with the Vidal gauge when excuting the tSU regauging iterations during the simulations for the heavy-hexagonal lattice consisting of $L = 133$ qubits, which corresponds to the results presented in Supplementary Figures 7 and 8. In this figure, each iteration of the tSU regauging process covers all the edges across the entire lattice. As the time step t/T progresses, the number of iterations required for achieving a fixed accuracy also increases. Nevertheless, even at $t/T = 100$, the convergence remains excellent with fewer than 30 iterations.

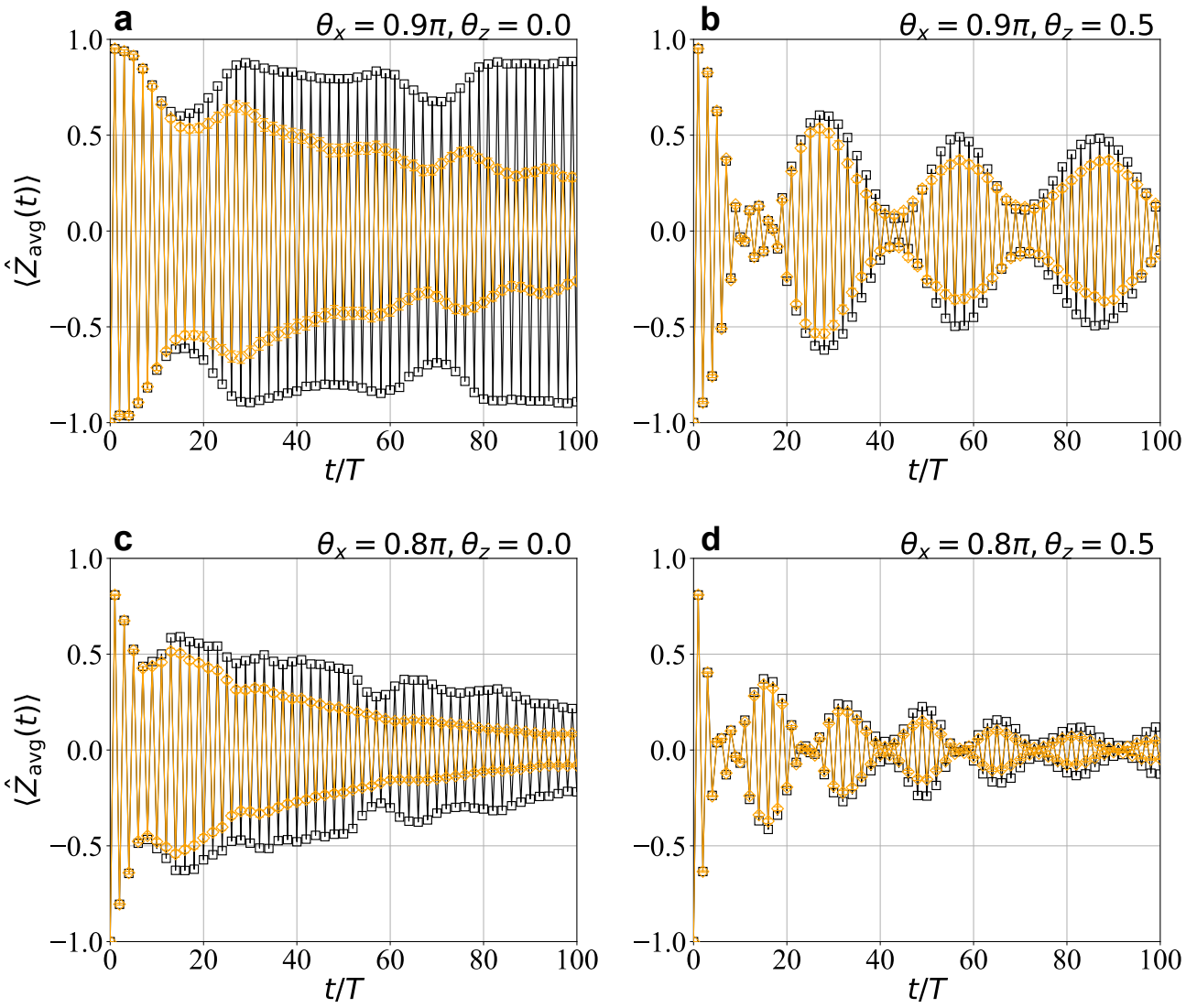

Supplementary Figure 19: Same as Supplementary Figure 18, but with $p_2 = 10p_1 = 0.005$.

[1] Seki, K. & Yunoki, S. Spatial, spin, and charge symmetry projections for a fermi-hubbard model on a quantum computer. Phys. Rev. A **105**, 032419 (2022). URL https://link.aps.org/doi/10.1103/PhysRevA.105.032419.

[2] Sun, R.-Y., Shirakawa, T. & Yunoki, S. Improved real-space parallelizable matrix-product state compression and its application to unitary quantum dynamics simulation. Phys. Rev. B **110**, 085149 (2024). URL https://link.aps.org/doi/10.1103/PhysRevB.110.085149.

[3] Tindall, J., Fishman, M., Stoudenmire, E. M. & Sels, D. Efficient tensor network simulation of ibm's eagle kicked ising experiment. PRX Quantum **5**, 010308 (2024). URL https://link.aps.org/doi/10.1103/PRXQuantum.5.010308.

[4] Kechedzhi, K. et al. Effective quantum volume, fidelity and computational cost of noisy quantum processing experiments. Future Generation Computer Systems **153**, 431–441 (2024). URL https://www.sciencedirect.com/science/article/pii/S0167739X23004569.

[5] Nielsen, M. A. & Chuang, I. L. Quantum Computation and Quantum Information: 10th Anniversary Edition (Cambridge University Press, 2010).

[6] Ippoliti, M., Kechedzhi, K., Moessner, R., Sondhi, S. & Khemani, V. Many-body physics in the nisq era: Quantum programming a discrete time crystal. PRX Quantum **2**, 030346 (2021). URL https://link.aps.org/doi/10.1103/PRXQuantum.2.030346.

[7] Vovrosh, J. et al. Simple mitigation of global depolarizing errors in quantum simulations. Phys. Rev. E **104**, 035309 (2021). URL

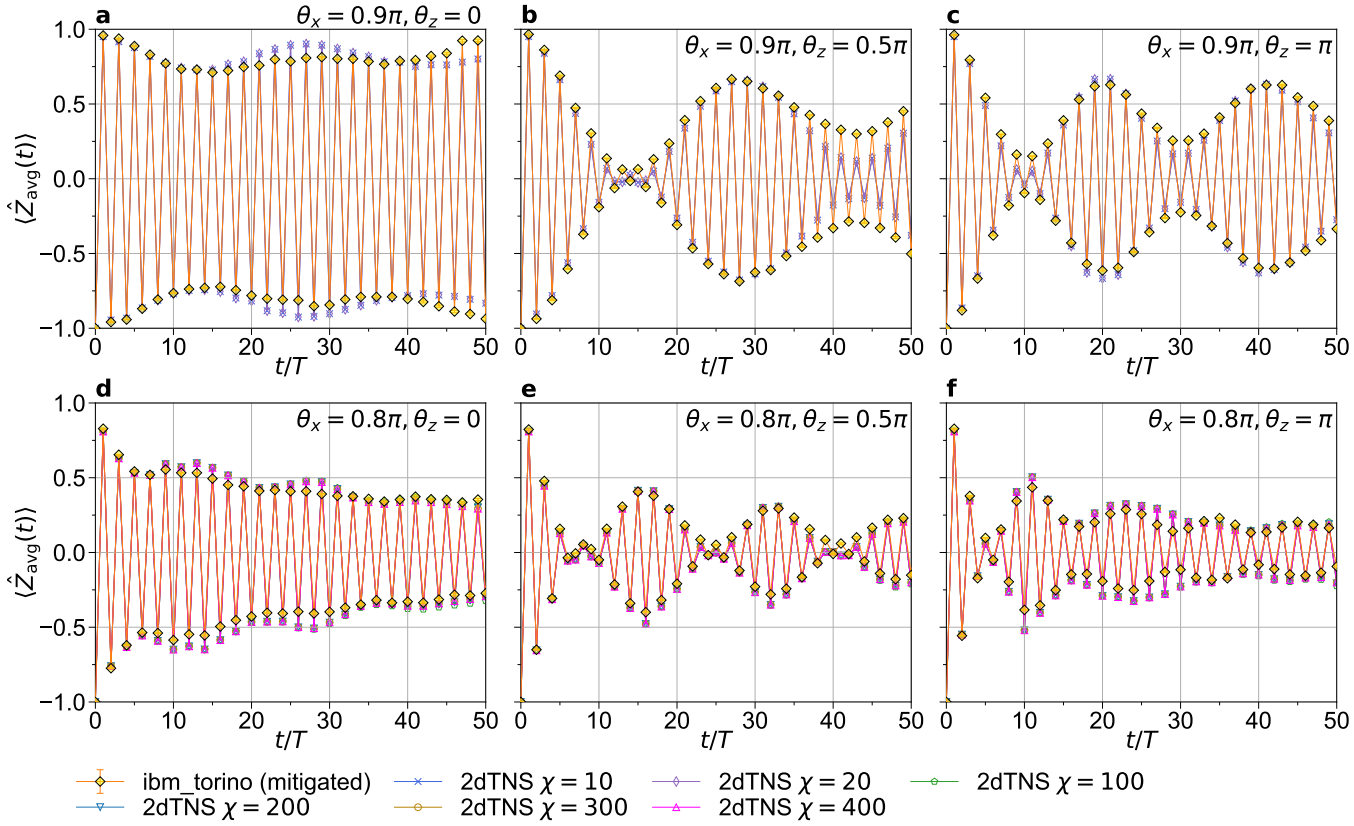

Supplementary Figure 20: Same as Supplementary Figure 8, but using the modified error mitigation protocol defined in Eq. (8).

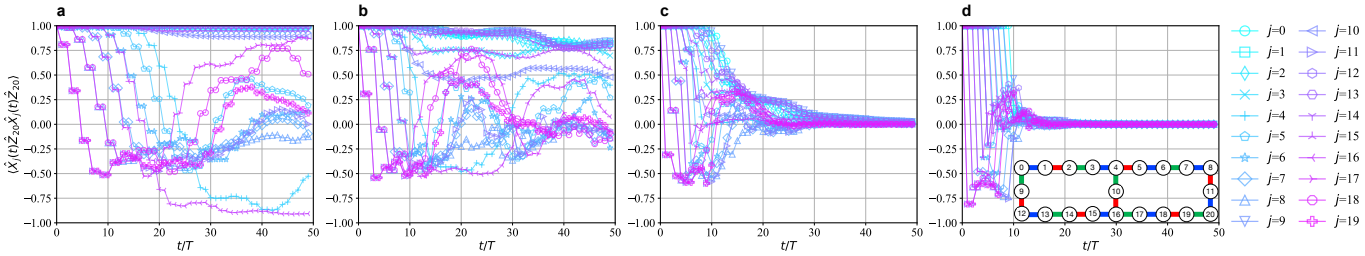

Supplementary Figure 21: Time evolution of the OTOC $\langle \hat{X}_j(t)\hat{Z}_{20}\hat{X}_j(t)\hat{Z}_{20} \rangle$ for the kicked Ising model on a heavy-hexagonal lattice of $L = 21$ qubits, obtained using the state-vector method. The positions of the qubits j are shown in **d**. The parameter θ_x is **a** 0.9π, **b** 0.8π, **c** 0.7π, and **d** 0.6π, with θ_z fixed at zero. Here, the initial state is prepared as a product state with all qubits set to $|0\rangle$, i.e., a fully-polarised state.

https://link.aps.org/doi/10.1103/PhysRevE.104.035309.

[8] Larkin, A. & Ovchinnikov, Y. N. Quasiclassical method in the theory of superconductivity. Sov. Phys. JETP **28**, 1200 (1969).

[9] Kitaev, A. & Suh, S. J. The soft mode in the sachdev-ye-kitaev model and its gravity dual (2018). 1711.08467.

[10] Hayden, P. & Preskill, J. Black holes as mirrors: quantum information in random subsystems. Journal of High Energy Physics **2007**, 120 (2007). URL https://dx.doi.org/10.1088/1126-6708/2007/09/120.

[11] Sekino, Y. & Susskind, L. Fast scramblers. Journal of High Energy Physics **2008**, 065 (2008). URL https://dx.doi.org/10.1088/1126-6708/2008/10/065.

[12] Deutsch, J. M. Quantum statistical mechanics in a closed system. Phys. Rev. A **43**, 2046–2049 (1991). URL https://link.aps.org/doi/10.1103/PhysRevA.43.2046.

[13] Srednicki, M. Chaos and quantum thermalization. Phys. Rev. E **50**, 888–901 (1994). URL https://link.aps.org/doi/10.1103/PhysRevE.50.888.

[14] Shinjo, K., Seki, K. & Yunoki, S. Emergent discrete time crystals on digital quantum computers: Boundary-protected and ancilla-induced disorder mechanisms of thermalization slowdown. arXiv preprint arXiv:2510.13577 (2025). URL https://doi.org/10.48550/arXiv.2510.13577.

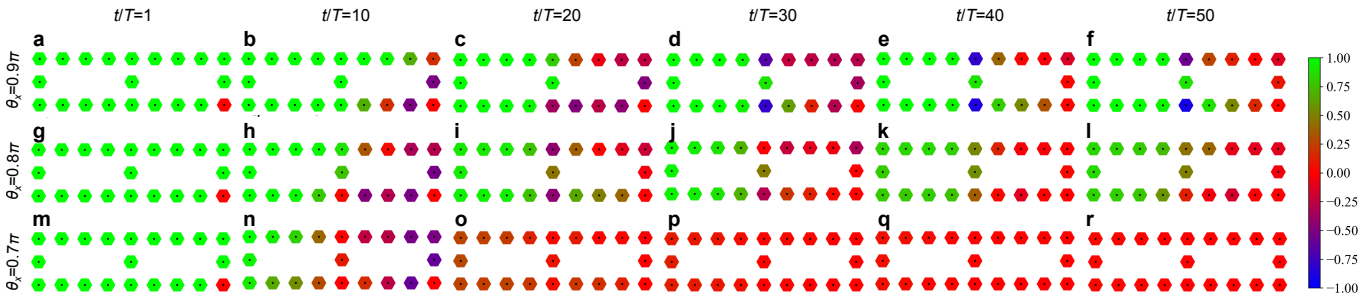

Supplementary Figure 22: Time evolution of the OTOC $\langle \hat{X}_j(t)\hat{Z}_{20}\hat{X}_j(t)\hat{Z}_{20}\rangle$ for the kicked Ising model on a heavy-hexagonal lattice of $L = 21$ qubits (see the inset of Supplementary Figure 21d). The parameter θ_x is **a**–**f** 0.9π, **g**–**l** 0.8π, and **m**–**r** 0.7π, with θ_z fixed at zero. Time steps t/T are; 1 for **a**, **g**, and **m**; 10 for **b**, **h**, and **n**; 20 for **c**, **i**, and **o**; 30 for **d**, **j**, and **p**; 40 for **e**, **k**, and **q**; and 50 for **f**, **l**, and **r**. Here, the initial state is prepared as a product state with all qubits set to $|0\rangle$, i.e., a fully-polarised state.

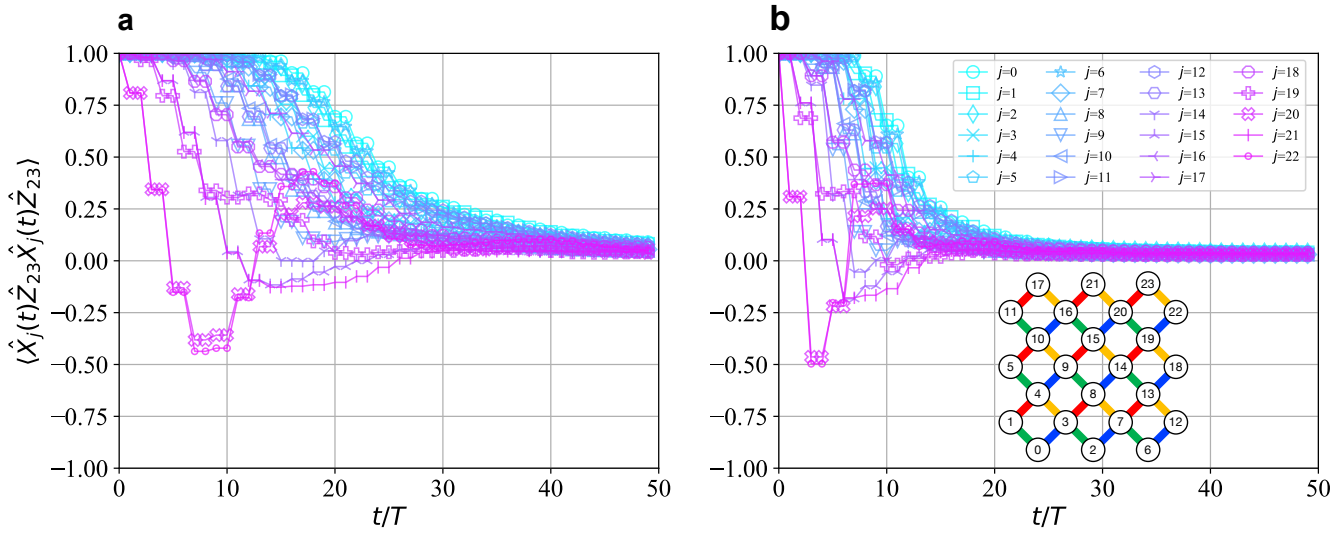

Supplementary Figure 23: Time evolution of the OTOC $\langle \hat{X}_j(t)\hat{Z}_{23}\hat{X}_j(t)\hat{Z}_{23}\rangle$ for the kicked Ising model on a square lattice of $L = 24$ qubits, obtained using the state-vector method. The positions of the qubits j are shown in **b**. The parameter θ_x is **a** 0.9π and **b** 0.8π, with θ_z fixed at zero. Here, the initial state is prepared as a product state with all qubits set to $|0\rangle$, i.e., a fully-polarised state.

[15] Mori, T., Kuwahara, T. & Saito, K. Rigorous bound on energy absorption and generic relaxation in periodically driven quantum systems. Phys. Rev. Lett. **116**, 120401 (2016). URL https://link.aps.org/doi/10.1103/PhysRevLett.116.120401.

[16] Else, D. V., Bauer, B. & Nayak, C. Prethermal phases of matter protected by time-translation symmetry. Phys. Rev. X **7**, 011026 (2017). URL https://link.aps.org/doi/10.1103/PhysRevX.7.011026.

[17] D'Alessio, L. & Polkovnikov, A. Many-body energy localization transition in periodically driven systems. Annals of Physics **333**, 19–33 (2013). URL https://www.sciencedirect.com/science/article/pii/S0003491613000389.

[18] Ponte, P., Chandran, A., Papić, Z. & Abanin, D. A. Periodically driven ergodic and many-body localized quantum systems. Annals of Physics **353**, 196–204 (2015). URL https://www.sciencedirect.com/science/article/pii/S0003491614003212.

[19] Vidal, G. Efficient classical simulation of slightly entangled quantum computations. Phys. Rev. Lett. **91**, 147902 (2003). URL https://link.aps.org/doi/10.1103/PhysRevLett.91.147902.

[20] Vidal, G. Efficient simulation of one-dimensional quantum many-body systems. Phys. Rev. Lett. **93**, 040502 (2004). URL https://link.aps.org/doi/10.1103/PhysRevLett.93.040502.

[21] Shi, Y.-Y., Duan, L.-M. & Vidal, G. Classical simulation of quantum many-body systems with a tree tensor network. Phys. Rev. A **74**, 022320 (2006). URL https://link.aps.org/doi/10.1103/PhysRevA.74.022320.

[22] Vidal, G. Classical simulation of infinite-size quantum lattice systems in one spatial dimension. Phys. Rev. Lett. **98**, 070201 (2007). URL https://link.aps.org/doi/10.1103/PhysRevLett.98.070201.

[23] Orús, R. & Vidal, G. Infinite time-evolving block decimation algorithm beyond unitary evolution. Phys. Rev. B **78**, 155117 (2008). URL https://link.aps.org/doi/10.1103/PhysRevB.78.155117.

[24] Nagaj, D., Farhi, E., Goldstone, J., Shor, P. & Sylvester, I. Quantum transverse-field ising model on an infinite tree from matrix product

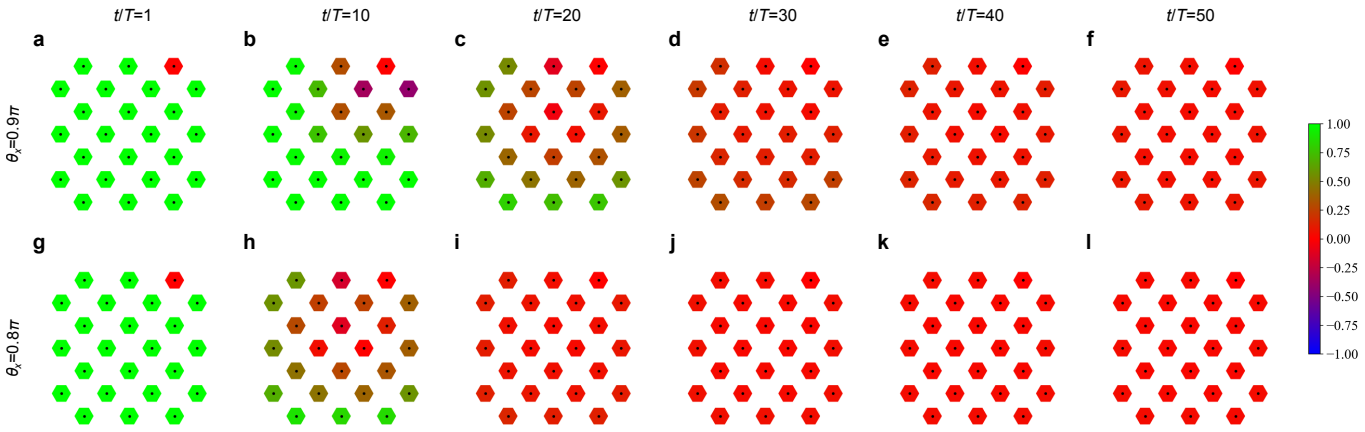

Supplementary Figure 24: Time evolution of the OTOC $\langle \hat{X}_j(t)\hat{Z}_{23}\hat{X}_j(t)\hat{Z}_{23}\rangle$ for the kicked Ising model on a square lattice of $L = 24$ qubits (see Supplementary Figure 23b). The parameter θ_x is **a**–**f** 0.9π and **g**–**l** 0.8π, with θ_z fixed at zero. Time steps t/T are: 1 for **a** and **g**; 10 for **b** and **h**; 20 for **c** and **i**; 30 for **d** and **j**; 40 for **e** and **k**; and 50 for **f** and **l**. Here, the initial state is prepared as a product state with all qubits set to $|0\rangle$, i.e., a fully-polarised state.

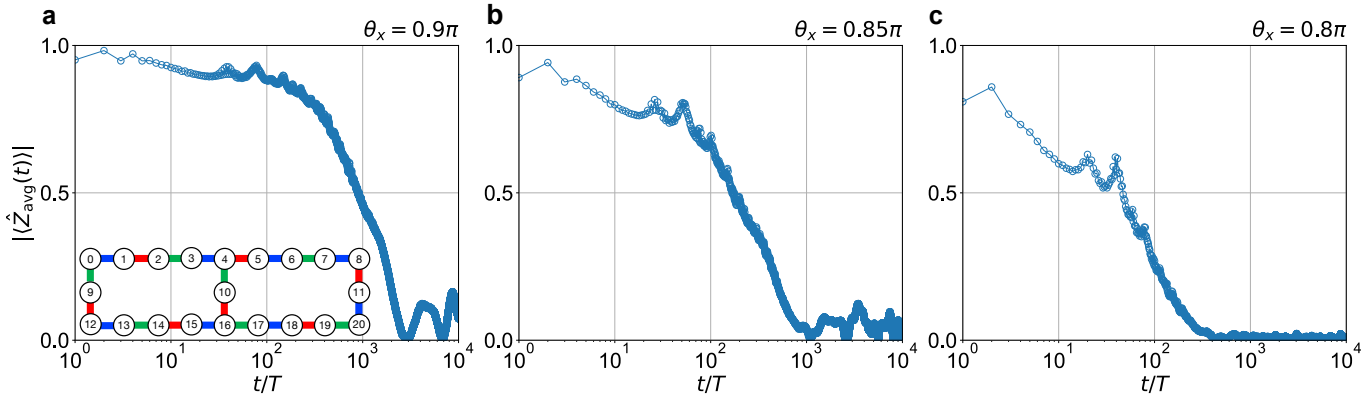

Supplementary Figure 25: Long-time evolution of the magnetisation $|\langle \hat{Z}_{\text{avg}}(t)\rangle|$ for the kicked Ising model on a heavy-hexagonal lattice of $L = 21$ qubits (see the inset in **a**), obtained using the state-vector method. The parameter θ_x is **a** 0.9π, **b** 0.85π, and **c** 0.8π, with θ_z fixed at zero. The average is taken over the entire systems, with the initial state prepared as a product state with all qubits set to $|0\rangle$, i.e., a fully-polarised state.

states. Phys. Rev. B **77**, 214431 (2008). URL https://link.aps.org/doi/10.1103/PhysRevB.77.214431.

[25] Kalis, H., Klagges, D., Or¥'us, R. & Schmidt, K. P. Fate of the cluster state on the square lattice in a magnetic field. Phys. Rev. A **86**, 022317 (2012). URL https://link.aps.org/doi/10.1103/PhysRevA.86.022317.

[26] Ran, S.-J., Li, W., Xi, B., Zhang, Z. & Su, G. Optimized decimation of tensor networks with super-orthogonalization for two-dimensional quantum lattice models. Phys. Rev. B **86**, 134429 (2012). URL https://link.aps.org/doi/10.1103/PhysRevB.86.134429.

[27] Phien, H. N., McCulloch, I. P. & Vidal, G. Fast convergence of imaginary time evolution tensor network algorithms by recycling the environment. Phys. Rev. B **91**, 115137 (2015). URL https://link.aps.org/doi/10.1103/PhysRevB.91.115137.

[28] Tindall, J. & Fishman, M. Gauging tensor networks with belief propagation. SciPost Phys. **15**, 222 (2023). URL https://scipost.org/10.21468/SciPostPhys.15.6.222.

[29] Jiang, H. C., Weng, Z. Y. & Xiang, T. Accurate determination of tensor network state of quantum lattice models in two dimensions. Phys. Rev. Lett. **101**, 090603 (2008). URL https://link.aps.org/doi/10.1103/PhysRevLett.101.090603.

[30] Corboz, P., Orús, R., Bauer, B. & Vidal, G. Simulation of strongly correlated fermions in two spatial dimensions with fermionic projected entangled-pair states. Phys. Rev. B **81**, 165104 (2010). URL https://link.aps.org/doi/10.1103/PhysRevB.81.165104.

[31] Jahromi, S. S. & Orús, R. Universal tensor-network algorithm for any infinite lattice. Phys. Rev. B **99**, 195105 (2019). URL https://link.aps.org/doi/10.1103/PhysRevB.99.195105.

[32] Leifer, M. & Poulin, D. Quantum graphical models and belief propagation. Annals of Physics **323**, 1899–1946 (2008). URL https://www.sciencedirect.com/science/article/pii/S0003491607001509.

[33] Poulin, D. & Bilgin, E. Belief propagation algorithm for computing correlation functions in finite-temperature quantum many-body systems on loopy graphs. Phys. Rev. A **77**, 052318 (2008). URL https://link.aps.org/doi/10.1103/PhysRevA.77.052318.

[34] Robeva, E. & Seigal, A. Duality of graphical models and tensor networks. Information and Inference: A Journal of the IMA

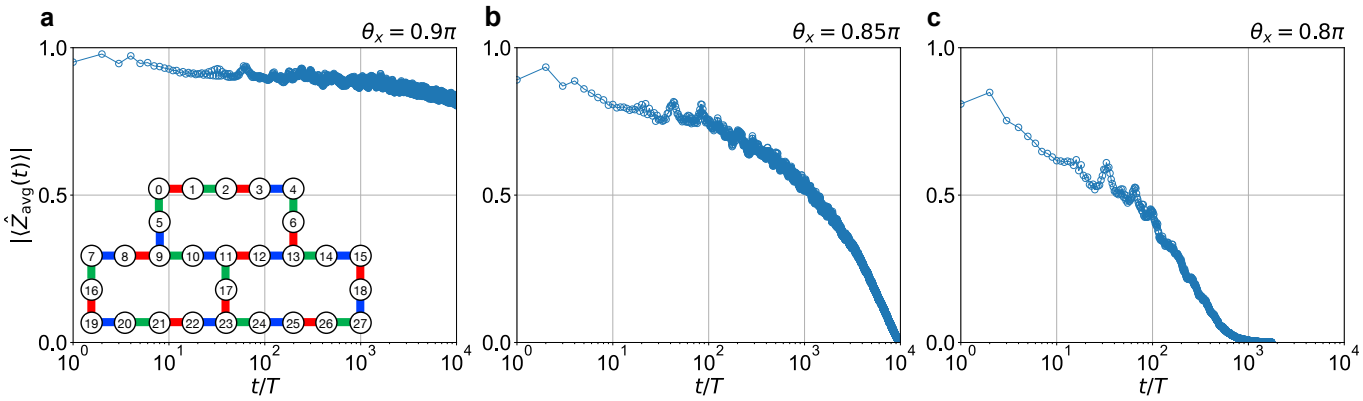

Supplementary Figure 26: Same as Supplementary Figure 25, but for a heavy-hexagonal lattice of $L = 28$ qubits (see the inset in **a**).

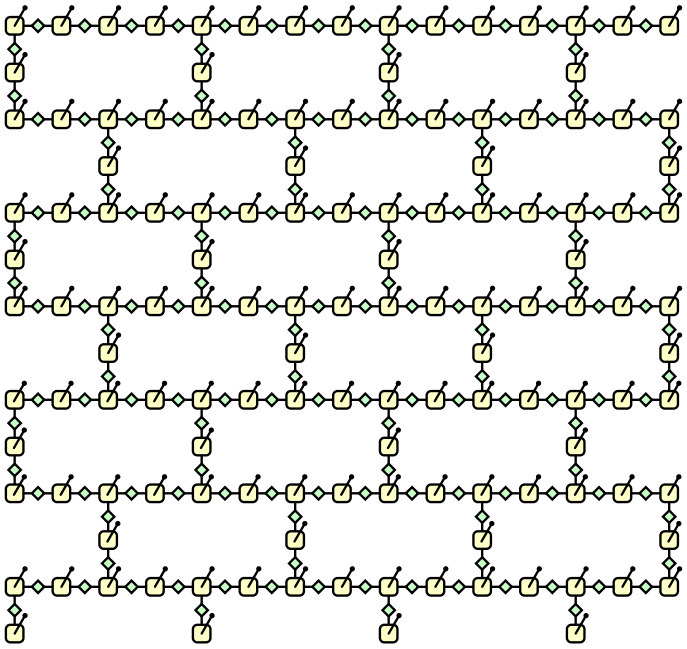

Supplementary Figure 27: Schematic structure of the two-dimensional gauging tensor network for the heavy-hexagonal lattice comprising $L = 133$ qubits. Edges represent virtual bonds with bond dimension χ. Vertex tensors, denoted as squares, have virtual bonds along with a physical bond representing qubit degrees of freedom. Gauge tensors, depicted as diamonds, are positioned on the edges connecting neighboring vertex tensors.

8, 273–288 (2018). URL https://doi.org/10.1093/imaiai/iay009. https://academic.oup.com/imaiai/article-pdf/8/2/273/28864933/iay009.pdf.

[35] Alkabetz, R. & Arad, I. Tensor networks contraction and the belief propagation algorithm. Phys. Rev. Res. **3**, 023073 (2021). URL https://link.aps.org/doi/10.1103/PhysRevResearch.3.023073.

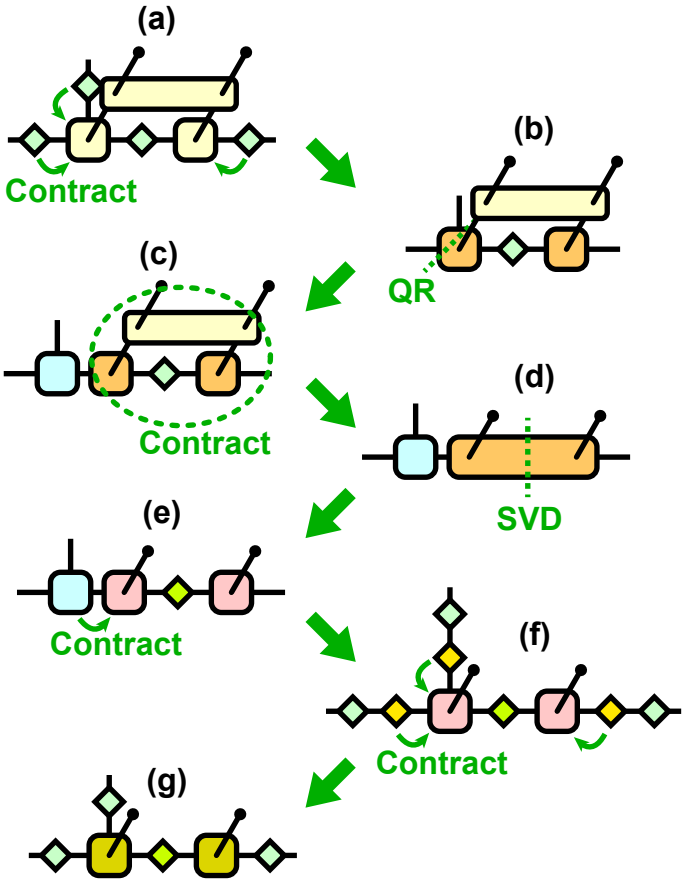

Supplementary Figure 28: A depiction of the time-evolved block decimation (TEBD) process for a TNS given in Supplementary Figure 27. (a) The surrounding gauge tensors are absorbed into the vertex tensors to which a two-qubit gate is applied. (b) QR decomposition is performed on the vertex tensor which has the three virtual bonds to reduce the computational cost for the following singular value decomposition (SVD) procedure. (c) All tensors connected to the two-qubit gate and the gauge tensor between the two vertex tensors are contracted. (d) SVD is performed on the tensor obtained in step (c). (e) The isometric tensor obtained from the QR decomposition in step (b) is incorporated into the new tensor obtained by SVD in step (d). (f) Inverses of the surrounding gauge tensors are computed and absorbed into the vertex tensors which have the physical bonds. (g) New tensors are obtained.

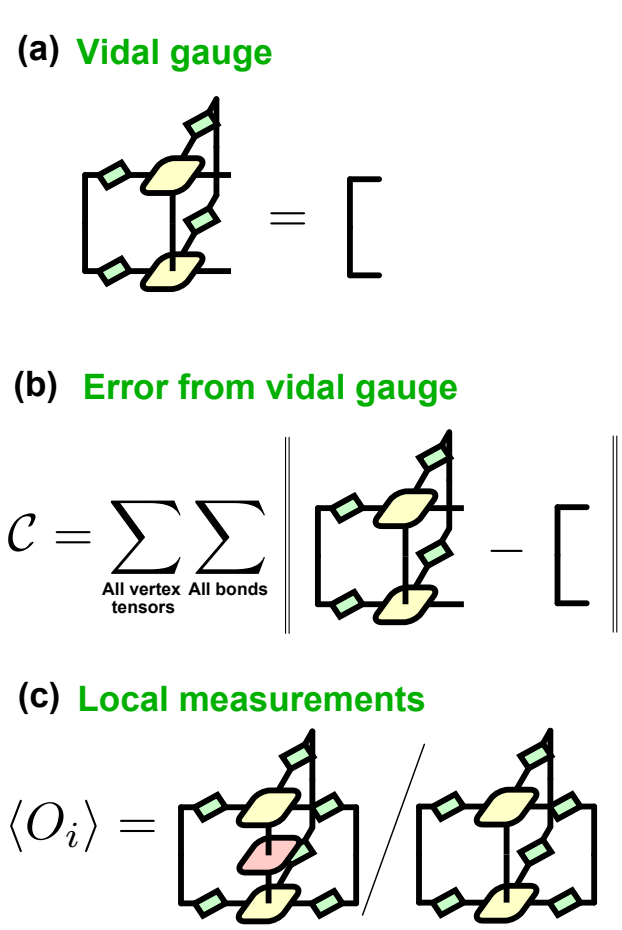

Supplementary Figure 29: (a) A TNS in the Vidal gauge satisfies the isometric condition after absorbing all but one of their neighboring gauge tensors around the vertex tensors. (b) Deviation from the Vidal gauge is quantified with C. Here, $\|\mathcal{A}\|$ represents the Frobenius norm for a tensor $\mathcal{A}$. Each tensor $\mathcal{A}$ after contraction is assumed to be normalised, i.e., $\tilde{\mathcal{A}} = \mathcal{A}/\|\mathcal{A}\|$. (c) Tensor contraction process for evaluating the expectation value $\langle \hat{O}_i \rangle$ of a local operator $\hat{O}_i$ (denoted as a red square), assuming that a TNS is in the Vidal gauge.

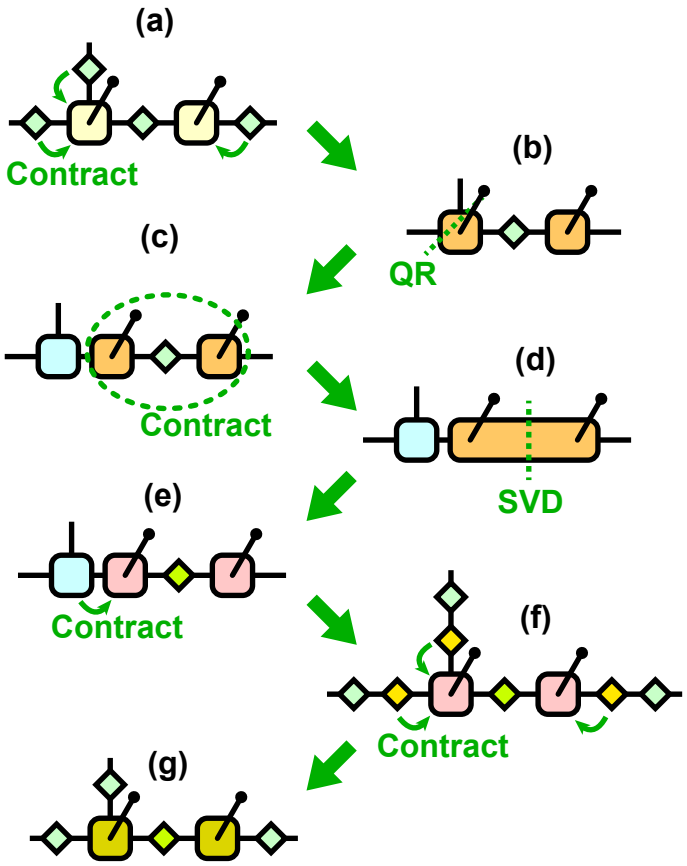

Supplementary Figure 30: Procedure for the trivial simple update (tSU), essentially equivalent to the process outlined in Fig 28, but without the inclusion of the two-qubit gate.

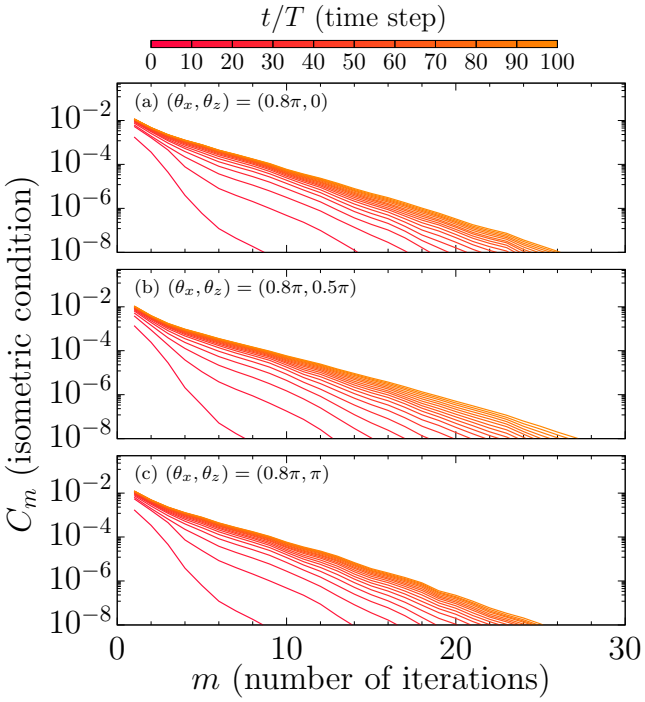

Supplementary Figure 31: Convergence to the Vidal gauge vs. the number m of iterations when employing the tSU regauging for the heavy-hexagonal lattice comprising $L = 133$ qubits. The parameters (θ_x, θ_z) are (a) $(0.8\pi, 0)$, (b) $(0.8\pi, 0.5\pi)$, and (c) $(0.8\pi, \pi)$. The bond dimension of the TNS is $\chi = 200$. C_m is the error from the Vidal gauge, defined as in Supplementary Figure 29(b), at iteration m, with color intensity denoting the time step t/T (indicated at the top). We set the error tolerance of 10^{-8} to ensure compliance with the Vidal gauge in our simulations.